Supplementary Information

Colloidal copper nanospheres boost propanol electrosynthesis from CO

Min Wang[a+], Anna Loiudice[a+], Enric Ibáñez Alé [b,c], Krishna Kumar,[a] Dragos Stoian,[d] Zan Lian[b], Petru Albertini[a], Ludovic Zaza[a], Jari Leemans[a], Núria López[b], Raffaella Buonsanti[a,*]

Synthetic methods

Materials. All chemicals were used as received, with no further purification. Tri-n-octylphosphine (TOP 98%), Tri-n-octylphosphine oxide (TOPO, 99%), Tetradecylphosphonic acid (TDPA, 98%), copper(I) bromide (CuBr, 99.999%), copper(I) acetate (Cu(OAc), 98%), commercial Cu nanopowder, 25 nm particle size (TEM), oleylamine (OLAM, 70%), tri-n-octylamine (TOA, 98%), toluene (anhydrous, 99.8%), hexane (anhydrous, 95%), octane (anhydrous, ≥99%), were purchased from Sigma-Aldrich. Copper(I) bromide (CuBr, 98%), Trioctylphosphine (TOP, 90%), oleylamine (OLAM, 80-90% C18 contents) were purchased from Acros Organics. Potassium hydroxide was purchased from REACTOLAB SA. Carbon paper (SIGRACET 39BC) and carbon cloth (W1S1010) for the fabrication of the electrodes were purchased from the Fuel Cell Store.

Methods

General consideration: All syntheses and manipulations of Cu NCs were performed under a dry N_2 atmosphere, using Schlenk-line techniques or a glove box. Anhydrous organic solvents were used for the manipulation, analysis and storage of Cu NCs. All volumes below 20 mL were measured and dispensed using Eppendorf microliter pipettes. All glassware were stored in oven at 110 °C to minimize air/moisture contamination.

Synthesis of colloidal Cu-Cube: Cu-Cubes were synthesized following the procedure introduced in our previous work.[1] TOPO (24 mmol, 9.37 g was first mixed with OLAM (117 ml) in a three-neck 250 ml flask equipped with reflux condenser and internal thermocouple temperature controller and degassed under vacuum with vigorous magnetic stirring at room temperature. CuBr (99.999% Sigma-Aldrich, 5 mmol, 0.71 g) was then added to the solution under N_2 flow. The resulting solution was rapidly (around ≈15 °C/min) heated to 260 °C and held at reflux at this temperature for 1 h before stopping the reaction and cooling down to room

temperature naturally. The solution was then transferred to a glove box by using glass vials kept under N_2 and divided into, 6 × 50 mL centrifuge tubes. Hexane (22 ml) was added to each tube and then centrifuged at 6000 rpm for 10 minutes. The precipitate was recovered in a minimal amount of hexane, an equal amount of ethanol was added, and then the resulting solution was centrifuged for an additional 10 minutes at 6000 rpm. The precipitate was finally recovered in 5 ml toluene and stored in a glove box.

Synthesis of colloidal Cu-S34: CuBr (98%, Acros Organics, 86 mg) and TOP (0.45 mL) were added to a 50 mL 3-neck flask in the glove box. The flask was sealed and was properly mounted and connected to a Schlenk line with reflux condenser and internal thermocouple temperature controller under N_2 flow. Afterwards, 7 mL OLAM were added to the flask. After adding the OLAM, the mixture turned greenish. The mixture was then degassed at 110 °C for 30 minutes under vacuum and another 30 minutes under N_2. Successively, the mixture was rapidly (around ≈15 °C/min) heated to 270 °C and held for 1 hour at this temperature. Finally, the mixture was cooled down naturally before being transferred to glass vial. The mixture was put in a 50 ml centrifuge tube and 20 ml of toluene was added. The particles were isolated by centrifugation at 6000 rpm for 10 minutes, and the supernatant was discarded. The particles were then washed using toluene (10 mL) and again isolated after centrifugation. The particles were redispersed in 5 mL toluene and were stored in an N_2 filled glovebox.

Synthesis of colloidal Cu-S80: Cu-S80 were synthesized with a similar procedure to Cu-S34 with slight variations. Specifically, the molar ratio of TOP to the Cu precursor allowed us to tune the size of the Cu spheres. Here, CuBr (98%, Acros Organics, 0.918 g) and TOP (3.5 mL) were added to a 250 mL 3-neck flask in a glove box. Afterwards, the flask was properly mounted and connected to the Schlenk line with reflux condenser and internal thermocouple temperature controller under N_2 flow. Then, 117 mL OLAM was added to the flask. Finally,

the conditions for the reaction regarding temperature/time, sample washing and storage in the glove box are the same as the Cu-S34 described above.

Synthesis of colloidal Cu-Octa: Cu-Octa were synthesized following the protocol adapted from Cu-S80. Controlling the heating ramp speed allowed us to tune the shape of the Cu NCs. Here, CuBr (98%, Acros Organics, 116 mg) and trioctylphosphine (TOP, 0.45 mL) were added to the 50 mL 3-neck flask in the glove box. Afterwards, the flask was properly mounted and connected to the Schlenk line with reflux condenser and internal thermocouple temperature controller under N_2 flowing with the same procedures as Cu-S80. Then, 15 mL OLAM (80-90%) was added to the flask. After adding the OLAM, the mixture turned greenish. The mixture was then degassed at 110 °C for 30 minutes, where the liquid became yellow-orange. After the mixture was kept another 30 mins at 110 °C but under N_2, the mixture was rapidly heated to 270 °C (heating ramp ≈30 °C/min) and hold for 1 hour. Finally, the mixture was cooled down naturally before being transferred to a glass vial. The mixture was put in a centrifuge tube and toluene was added to get an end volume of approx. 30 mL. The particles were isolated by centrifugation at 6000 rpm for 10 minutes, and the supernatant was discarded. The particles were then washed using toluene (10 mL) and isolated after centrifugation. The particles were redispersed and combined into a single suspension using 5 mL toluene and were stored in an N_2 filled glovebox.

Synthesis of colloidal Cu-S7: Cu-S7 were synthesized following a protocol adapted from previous procedures.[2] In a 50 mL 3-necked round bottom flask equipped with a condenser, a thermocouple, a septum and an olive shaped teflon stirrer, TOA (20 mL) was introduced at room temperature and then degassed under dynamic vacuum at 130 ºC for 1 hour. The flask was then refilled with N_2 gas and cooled to 50 ºC. TDPA (270 mg, 1 mmol) and Cu(OAc) (245 mg, 2 mmol) were added to the flask in the form of a powder, forming a green, cloudy mixture. The mixture was heated to 180 °C and kept at this temperature for 30 minutes. After this time,

the mixture was heated to 270 °C. The reaction was hold at this temperature for 30 minutes and then allowed to cool down to room temperature by removing the heating mantle. The reaction mixture was transferred into 40 mL glass vials with a septum filled with N_2. To each 5 mL portion of the crude reaction mixture, hexane (5 mL) and ethanol (15 mL) were added. The particles were isolated by centrifugation at 13500 rpm for 10 minutes, and the supernatant was discarded. The collected pellet was then washed using hexane (5 mL) and ethanol (10 mL) and again isolated after centrifugation. Finally, the particles were redispersed and combined into a single suspension using 15 mL toluene and were stored in an N_2 filled glovebox.

Synthesis of colloidal Cu-S4: Cu-S4 were synthesized following the same procedure of Cu-S7 with slight variations. After setting up the reaction following the procedure described above, the temperature of the reaction mixture was first set to 180 °C for 30 minutes, then to 230 °C and the reaction is stopped as soon as the set temperature is reached. The reaction mixture was transferred into 40 mL glass vials with a septum filled with N_2. Afterwards, the solution is transferred in a centrifuge tube and 20 mL of ethanol are added. After centrifugation at 13000 rpm for 10 minutes, the precipitate was discarded because it contains unreacted lamella.[2] The colored supernatant is split in two centrifuge tubes, further centrifugated after addition of 10 mL of extra ethanol. The collected precipitate is washed again using hexane (5 mL) and ethanol (5 mL) and isolated by centrifugation. Finally, the precipitate was redispersed and combined into a single suspension using 5 mL toluene and was stored in an N_2 filled glovebox.

The Cu concentration of all the above Cu NCs stock solution was measured by Inductively Coupled Plasma Optical Emission Spectrometry (ICP-OES). A typical concentration was around 10 - 15 mg/mL of Cu.

Additional materials characterizations

Inductively Coupled Plasma Optical Emission Spectrometry (ICP-OES): was performed on an Agilent 5100 model to determine the solution concentration of synthesized Cu NCs and the Cu loading on GDEs. The sample solution was prepared by digesting overnight in 70% ICP grade HNO_3 followed by opportune dilution with DI water to obtain a 2% acid content needed for the analysis.

Scanning electron microscopy (SEM): cross section SEM images were acquired on a FEI Teneo, using an inlens (Trinity) detector and EDX detector.

X-Ray diffraction (XRD): The XRD data on the GDL of the as-prepared and post CORR were acquired with Bruker D8 Advance diffractometer with a Cu Kα source equipped and a Lynxeye one-dimensional detector. The XRD data used in **Supplementary Fig. 23** were acquired at the Swiss-Norwegian beamlines BM31 at the European Synchrotron Radiation Facility in Grenoble, France using a sagittal focusing second crystal. The X-ray was applied in a focused beam and shaped to *ca.* 50 μm (horizontal) and 2-300 μm (vertical) via the uses of slits. PILATUS3 X CdTe 2M was used as a detector. The Cu NCs were measured in solution sealed capillaries (1.5 mm o.d., 10 μm wall thickness). The fits were done with TOPAS6 using the Rietveld method. The instrumental resolution function was determined empirically on a LaB6 standard modelling a Split-PearsonVII function which described peak shapes the best. A Chebychev polynomial of order 6 was used to model the background of sample data. Lattice parameters, scale factor and one isotropic displacement parameter per atom were refined per phase. Size broadening was modelling with a Gaussian and Lorentzian component. A satisfactory fit using only one or the other could not describe the angle-dependent size broadening. Microstrain broadening was modeled using one Lorentzian or Gaussian

contribution, and crosschecked with results using both contributions. All approaches yielded similar microstrain parameters.

X-ray photoelectron spectra (XPS): were recorded using an Axis Supra (Kratos Analytical) instrument, using the monochromated Kα X-ray line of an Al anode. The pass energy was set to 40 eV with a step size of 0.15 eV. The samples were electrically insulated from the sample holder and charges were compensated. Spectra were referenced at 284.8 eV using the C–C bound of the C 1s orbital.

Electrocatalytic Measurements: Electrodes were prepared by air brushing NCs solutions on the micro-porous layer of the carbon paper with area of 1.33 cm^2. For the stability test a modified carbon cloth was used fabricated as reported previously.[3] Cu NCs air brushing was performed by diluting a concentrated solution of NCs in hexane to obtain 1.5 ml of solution having a higher content of NCs than the desired amount. This is necessary because we evaluated by ICP measurements that only 33-35% (Cu-Cube, Cu-Octa, Cu-S80 and Cu-S34) or 70% (Cu-S7) of the active content is deposited on the substrate. So, 3 times of the desired amount for Cu-Cube, Cu-Octa, Cu-S80 and Cu-S34 were diluted in 1.5 mL hexane. 1.4 times of the desired amount for Cu-S7 were also diluted in 1.5 mL hexane. The obtained solution is sonicated for few seconds to disperse the NCs, then immediately sprayed on the GDL. The obtained GDEs were allowed to dry and then stored in controlled atmosphere until use.

Electrochemical characterization and products analysis: Electrochemical characterizations were performed in a flow cell electrolyzer having a geometry like those reported in literature.[4] Ag/AgCl electrode (leak free series, Innovative Instruments, Inc.) were used as the reference electrode, and anionic exchange membrane (Fumasep FAB-PK-130) was interposed between the anolyte and the catholyte compartments, as counter electrode a nickel mesh (Mc Master–Carr, 100x100 mesh size) was used. Anolyte and catholyte solutions (40 ml each) were

circulated in both the compartments by means of a dual-channel peristaltic pump (FAUST PLP380) at a constant flow 1 ml/min. High purity CO or gas mixture ($CO:N_2$) was purged in the back chamber of catholyte compartment at a constant flow 10 mL/min or 60 mL/min by mean of a digital mass flow controller (Bronkhorst). The electrocatalytic measurements were performed by applying currents in a range from 100 to 300 mA/cm^2 using a potentiostat Biologic SP-300. The CO flow at outlet from the electrochemical flow cell was constantly measured with an ADM flow meter (Agilent CrossLab CS) and used for the FE calculations to avoid any carbon balance issue.[5]

For the analysis of gaseous products, a gas chromatograph (GC 8610C, SRI instruments) equipped with a HayeSep D porous polymer column, thermal conductivity detector, and flame ionization detector was used. Gas sampling was performed at regular intervals of 10 minutes. Ultra-high purity N_2 (99.999%) was used as a carrier gas. The concentration of gaseous products was determined using calibration curves from standard gas mixtures. For liquid product analysis, high-performance liquid chromatography (HPLC) or NMR was used. HPLC was carried out on an UltiMate 3000 instrument from Thermo Scientific. 5 mM H_2SO_4 was used as the eluent for the HPLC measurements. NMR was carried out on a Bruker Avance III HD 400 MHz 9.4 T spectrometer equipped with a 5 mm BBFO liquid probe. ^1H NMR spectra were acquired using a standard pulse sequence from the Bruker library that allowed water suppression. The quantitative 1D HNMR spectra were recorded with 30 s relaxation delay (d1) to allow full relaxation of the internal standard (DMSO). We note that the total FE is below 100% for samples where acetate is the major product (i.e. cubes and octahedra). A similar observation can be made in other studies where acetate is the major CORR product.[6,7] Actually we observe a trend where the higher the FE of acetate is, the more the FE deviates from 100% (**Fig. 1b and Supplementary Fig. 3**). One possible explanation is the difficulty in detecting

the highly volatile acetaldehyde. Acetaldehyde is a CORR product which transform into acetate via fast non-Faradaic chemical oxidation in alkaline environments.[8,9]

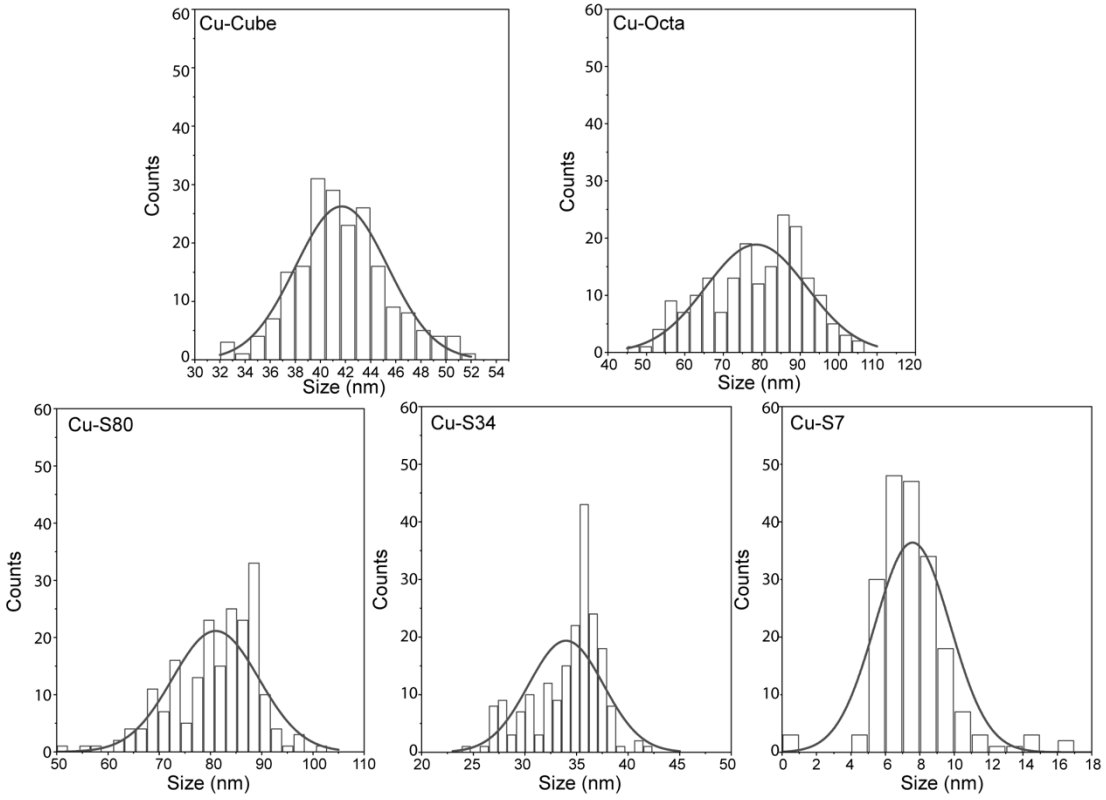

Supplementary Fig. 1 Size histograms for Cu-Cube, Cu-Octa, Cu-S80, Cu-S34 and Cu-S7. The size of Cu-Octa corresponds to the edge length. The size of the spheres is the diameter.

Supplementary Table 1. Size, volume and surface area of the studied Cu NCs.

Sample name	Size* (nm)	r (nm)	Volume (V) (nm^3)	Surface area (S) (nm^2)	S/V
Cu-Cube	41.7±3.7		72511.7	10433.3	0.1
Cu-Octa	78.6±13.1		228646.2	21384.7	0.1
Cu-S80	81.0±8.4	40.5	278120.8	20601.5	0.1
Cu-S34	34.0±3.6	17.0	20569.1	3629.8	0.2
Cu-S7	7.6±2.2	3.8	227.0	179.9	0.8
Cu-S4	4.1±0.7	2.0	35.4	52.2	1.5

*The size of the spheres is the diameter, the size of the octahedra and cube is the edge.

Supplementary Table 2: FEs for all the different Cu catalysts tested in this work for CORR at 100 mA/cm^2 in 0.5 M KOH and corresponding measured half-cell potential (E) vs Ag/AgCl and corrected potential (E_{corr}) vs RHE. Error bars represent the standard deviation of three independent samples.

	FE_{H2} (%)	FE_{CH4} (%)	FE_{C2H4} (%)	FE_{AcO-} (%)	FE_{EtOH} (%)	FE_{n-PrOH} (%)	J_{n-PrOH} (mA/cm^2)	E (V vs Ag/AgCl)	E_{corr}* (V vs RHE)
Cu-Cube	**5.3**	**1.3**	**19.8**	**39.8**	**18.4**	**3.3**	**3.3**	**-2.46**	**-0.79**
STDV.	0.8	1.7	2.4	6.7	6.9	3.0		0.10	0.10
Cu-Octa	**8.9**	**6.2**	**17.7**	**26.3**	**18.1**	**5.1**	**5.1**	**-2.45**	**-0.87**
STDV.	2.4	2.7	1.6	1.2	1.7	2.0		0.08	0.08
Cu-S80	**18.3**	**0.3**	**23.4**	**13.6**	**29.2**	**19.7**	**19.7**	**-2.39**	**-0.81**
STDV.	2.9	0.2	1.3	1.9	1.7	2.3		0.10	0.10
Cu-S34	**14.2**	**0.5**	**21.6**	**18.7**	**28.7**	**14.1**	**14.1**	**-2.36**	**-0.77**
STDV.	0.5	0.1	3.4	1.1	±0.6	1.6		0.08	0.08
Cu-S7	**10.2**	**-**	**22.1**	**8.1**	**33.7**	**23.0**	**23.0**	**-2.27**	**-0.75**
STDV.	3.4		1.8	1.4	4.3	6.1		0.06	0.06
Cu-S4	**10.9**	**0.4**	**11.5**	**25.8**	**14.5**	**34.8**	**34.8**	**-2.39**	**-0.80**
STDV.	1.4	0.5	2.3	1.5	2.0	1.4		0.04	0.04
Cu-Comm	**26.8**	**5.0**	**14.1**	**17.9**	**18.7**	**8.6**	**8.6**	**-2.47**	**-0.83**
STDV.	2.3	1.2	1.8	2.6	3.5	4.8		0.04	0.04

***** E_{corr} is calculated as previously reported[10] using this formula:

$$E_{corr} = E + 0.206 + 0.0591*pH - 0.85*iR_{drop}$$

where E is the measured potential vs Ag/AgCl, pH is fixed to 14, *i* is the applied current and R_{drop} is measured at the end of each experiment via electrochemical impedance spectroscopy. A factor of 0.85 is used for the correction term because the 0.5 M KOH electrolyte has a low resistivity and holds a relatively low voltage drop over the electrolyte; the drift of the reference electrode was also included in the calculations.

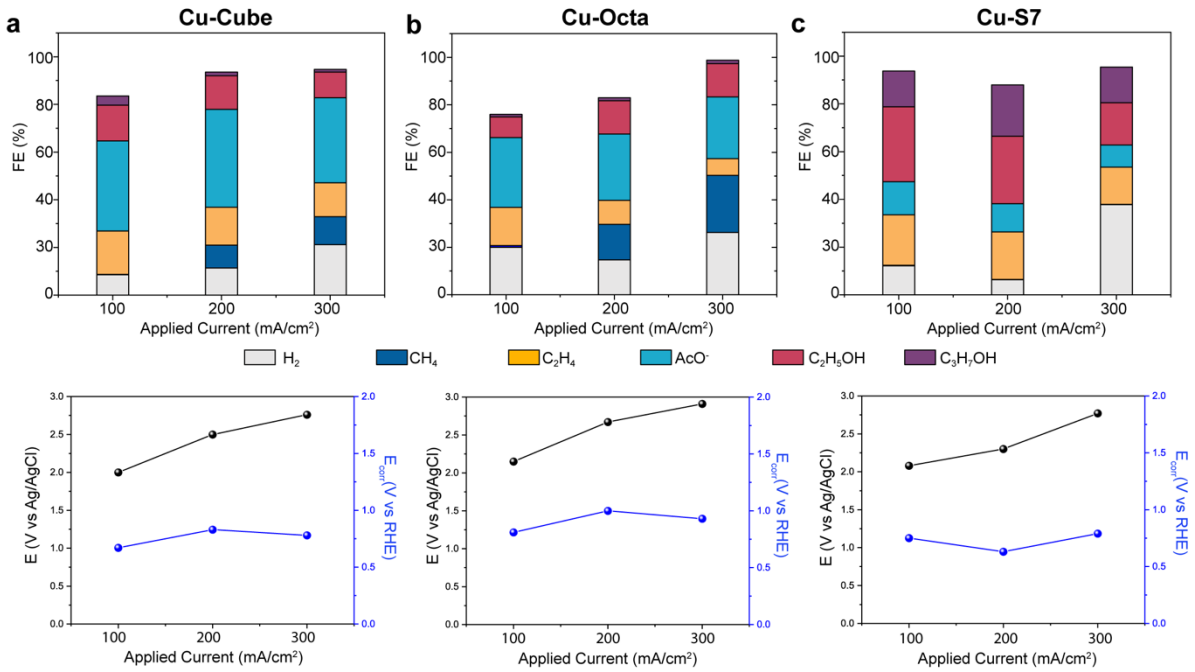

Supplementary Fig. 2 Total FEs for CORR in 1 M KOH at different applied current densities (top) (100 mA/cm^2, 200 mA/cm^2 and 300 mA/cm^2) and corresponding measured potential (E) vs Ag/AgCl and iR_{drop} corrected potentials (E_{corr}) vs RHE (bottom) for (a) Cu-Cube, (b) Cu-Octa and (c) Cu-S7.

The measured potentials for all the different Cu catalysts at various applied currents are in the same range, proving that the observed trends in selectivity among them are not due to potential-dependence of the product distribution.

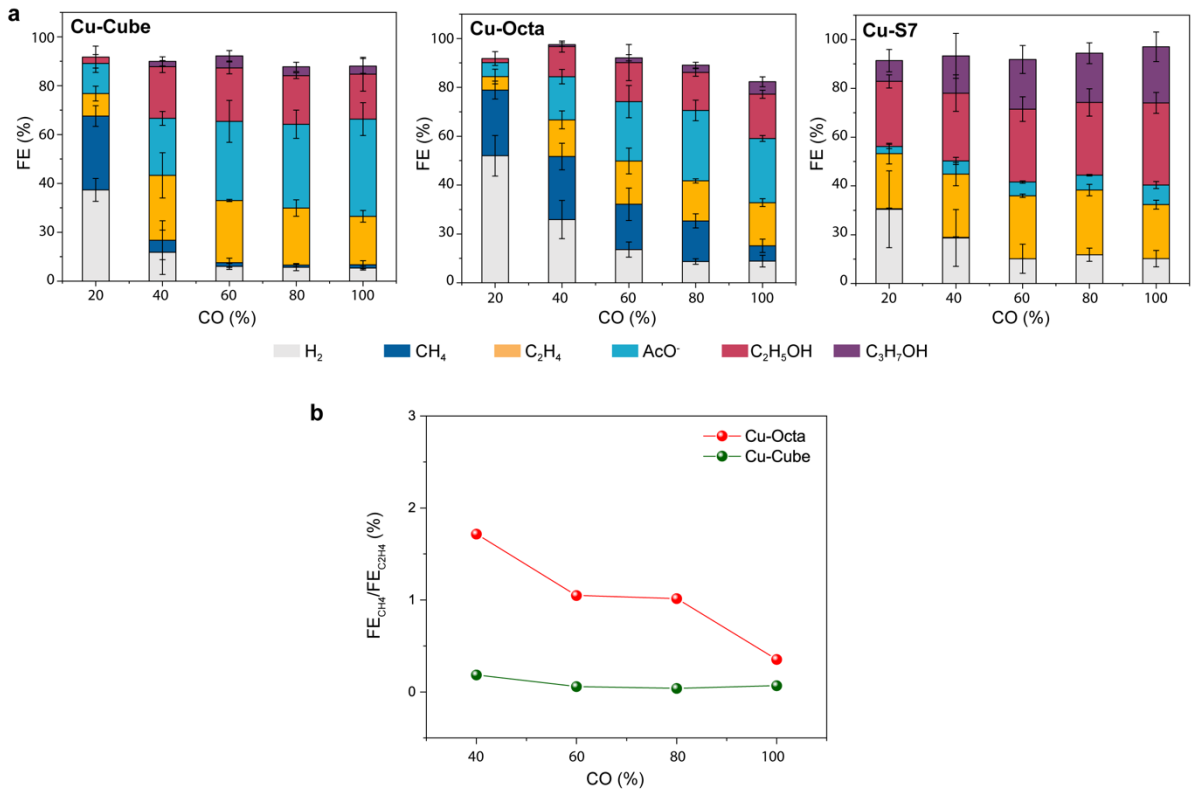

Supplementary Fig. 3 a, FEs of all products at different CO concentration in an inert N_2 carrier gas at 100 mA/cm^2 in the flow-cell using 0.5 M KOH as the electrolyte for Cu-Cube, Cu-Octa and Cu-S7. The reported values are an average of three independent experiments with error bars indicating the standard deviations. **b,** Ratio of the FE for CH_4 and C_2H_4 for Cu-Cube and Cu-Octa at the different CO coverage. This plot highlights the increase of methane for the Cu-Octa at low CO coverage compared to Cu-Cube, where the amount of methane compared to ethylene remain negligible.

Supplementary Note 1: Catalyst morphology and composition post and during CORR

XRD and electron microscopy show that the structure of the catalysts does not change after 1 hour of CORR (**Supplementary Fig. 4**).

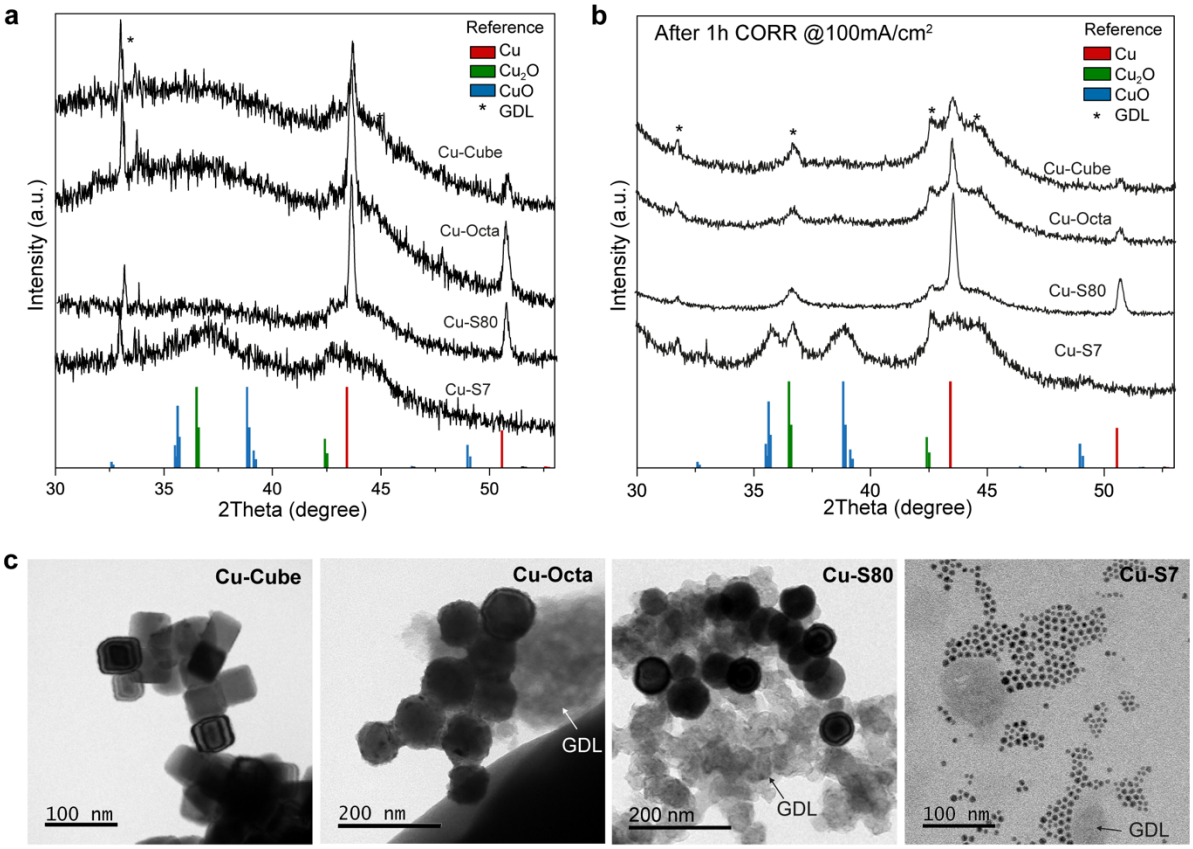

Supplementary Fig. 4 XRD patterns of (a) as-prepared and (b) after 1h CORR at 100 mA/cm^2 in 0.5 M KOH for Cu-cube, Cu-octa, Cu-S80 and Cu-S7 on GDL. (c) TEM images of the sample in (b).

We also performed operando X-ray absorption spectroscopy (XAS) of all tested Cu NCs to assess their composition and eventual changes during CORR (**Supplementary Figs. 5-7**). The X-ray absorption near-edge spectroscopy (XANES) profiles of the Cu K-edge indicate a mixture a copper species (Cu^0, Cu^+ and Cu^{2+}) at open circuit potential (OCP) for all samples (**Supplementary Fig. 5,6**). The fraction of oxidized copper species increases as the surface-to-volume ratio increases; Cu-S7 are completely oxidized, which is consistent with our previous studies. [11]

As the cathodic current is applied, the fraction of oxidized copper is reduced for all samples. The amount of Cu^{2+} and Cu^+ is higher for the Cu-S7 compared to the other samples, although with a fraction below 20%. The possibility of the copper speciation impacting the selectivity

towards n-propanol exists. However, the fact that Cu-Cube, Cu-Octa and Cu-S80 turn into purely metallic copper during CORR, yet only the Cu-S80 are more selective for alcohols, indicates the contribution of copper oxidation cannot be the major reason behind the selectivity observed for the spherical Cu catalysts. Furthermore, we performed additional control experiments, which are reported in **Supplementary Fig. 8**. Here, we purposely oxidized the surface of the cubes using a hydrogen peroxide treatment, which we recently developed.[11] This oxidation did not lead to any change in the product selectivity.

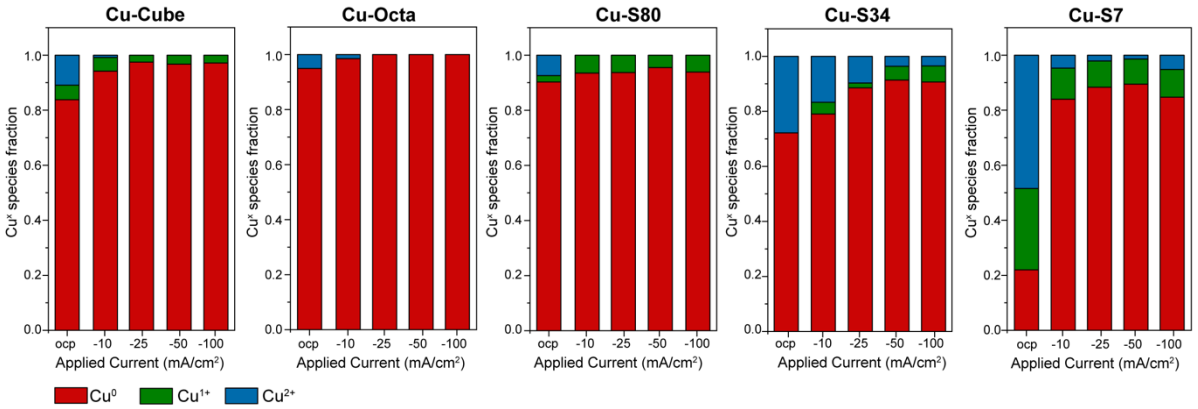

Supplementary Fig. 5 Linear combination analysis (LCA) for the tested Cu NCs acquired in operando under different applied currents using the LCA.

Cu foil, Cu_2O and CuO standards reported in the Supplementary Fig. 6 were used to build the LCA models (**Supplementary Fig. 7**).

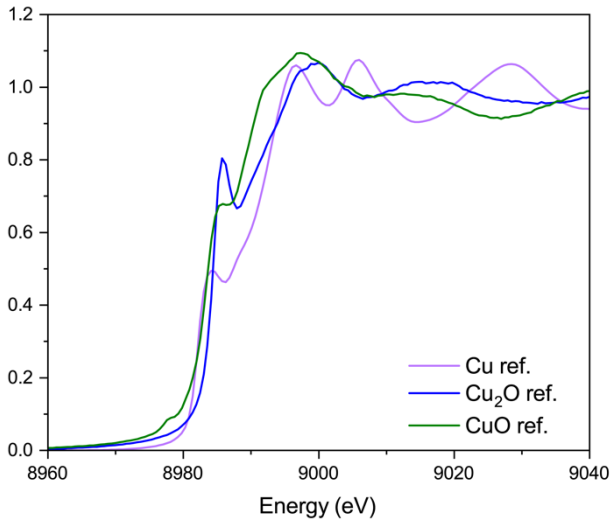

Supplementary Fig. 6 Cu K-edge XANES spectra of Cu, Cu_2O and CuO commercial bulk references.

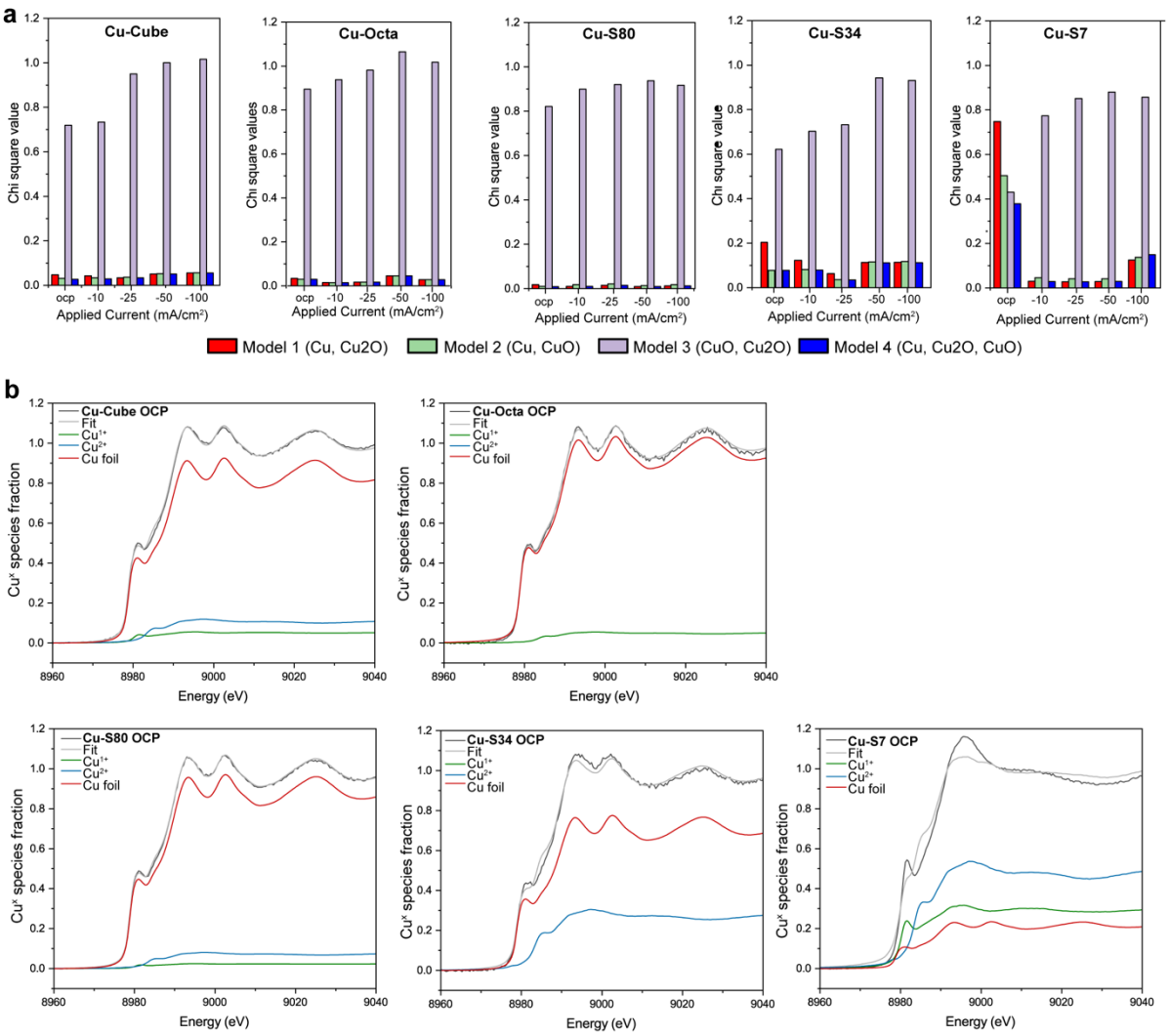

Supplementary Fig. 7 LCA Analysis on the XANES spectra. a, Evolution of chi square values as a function of the applied current for the Cu-Cube, Cu-Octa, Cu-S80, Cu-S34 and Cu-S7 catalysts and the four LCA models evaluated based on the bulk standards reported in **Supplementary Fig. 6**. **b,** Example of as-acquired XANES spectra together with the fitted spectra using Model 4 for the Cu-Cube, Cu-Octa, Cu-S80, Cu-S34 and Cu-S7 catalysts measured at OCP in 0.5 M KOH as electrolyte.

The XANES data were reduced and normalized using the Larch package. The four LCA models were built by considering different components of copper oxides, as indicated in the legend of the figure. At OCP, Model 3, which exclude the presence of metallic copper, is not applicable for any of the systems, as it is the one with the highest chi square. This result indicates that the metallic copper component must be included at OCP. Models 1, 2 or 4 can all be applied with statistically insignificant differences for Cu-Cube, Cu-Octa and Cu-S80 at OCP. Instead, Cu-S34 and Cu-S7 are best modeled by assuming a mixed of Cu^0, Cu^+ and Cu^{2+}, as the chi square corresponding to Model 4 is smaller compared to Model 1 to 3 (**Supplementary Fig. 7a**), which is consistent with a higher oxide fraction due to higher surface to volume ratio. The oxidation can be caused by contact with the aqueous electrolyte or unavoidable exposure to air.

As the applied current become more negative, the difference between Model 1 and the other Models becomes almost insignificant for all systems which indicates that the oxide fractions get reduced. Nevertheless, the Model 4 is the one with the lowest chi square at OCP for all systems, therefore this model was picked for the analysis in **Supplementary Fig. 5**.

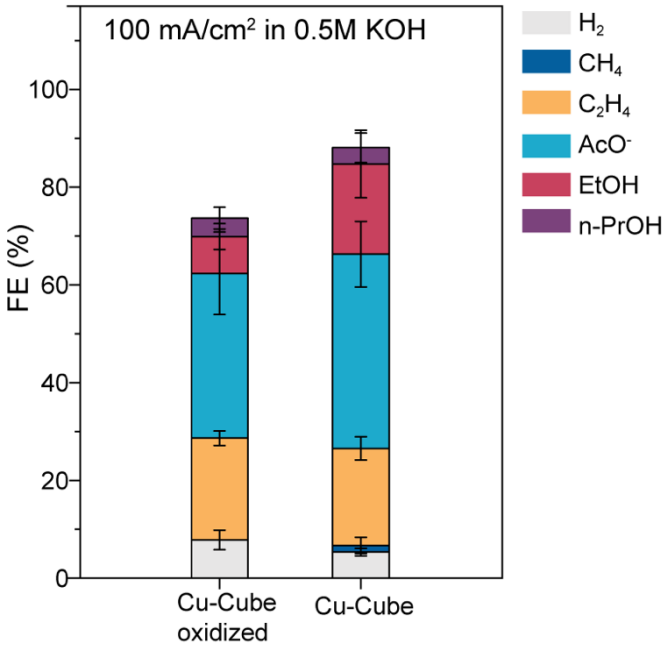

Supplementary Fig. 8 FE efficiency of oxidized Cu-Cube showing similar performance to the as-prepared Cu-Cube. Cu-Cube were oxidized on the surface via a mild surface treatment with hydrogen peroxide.[11]

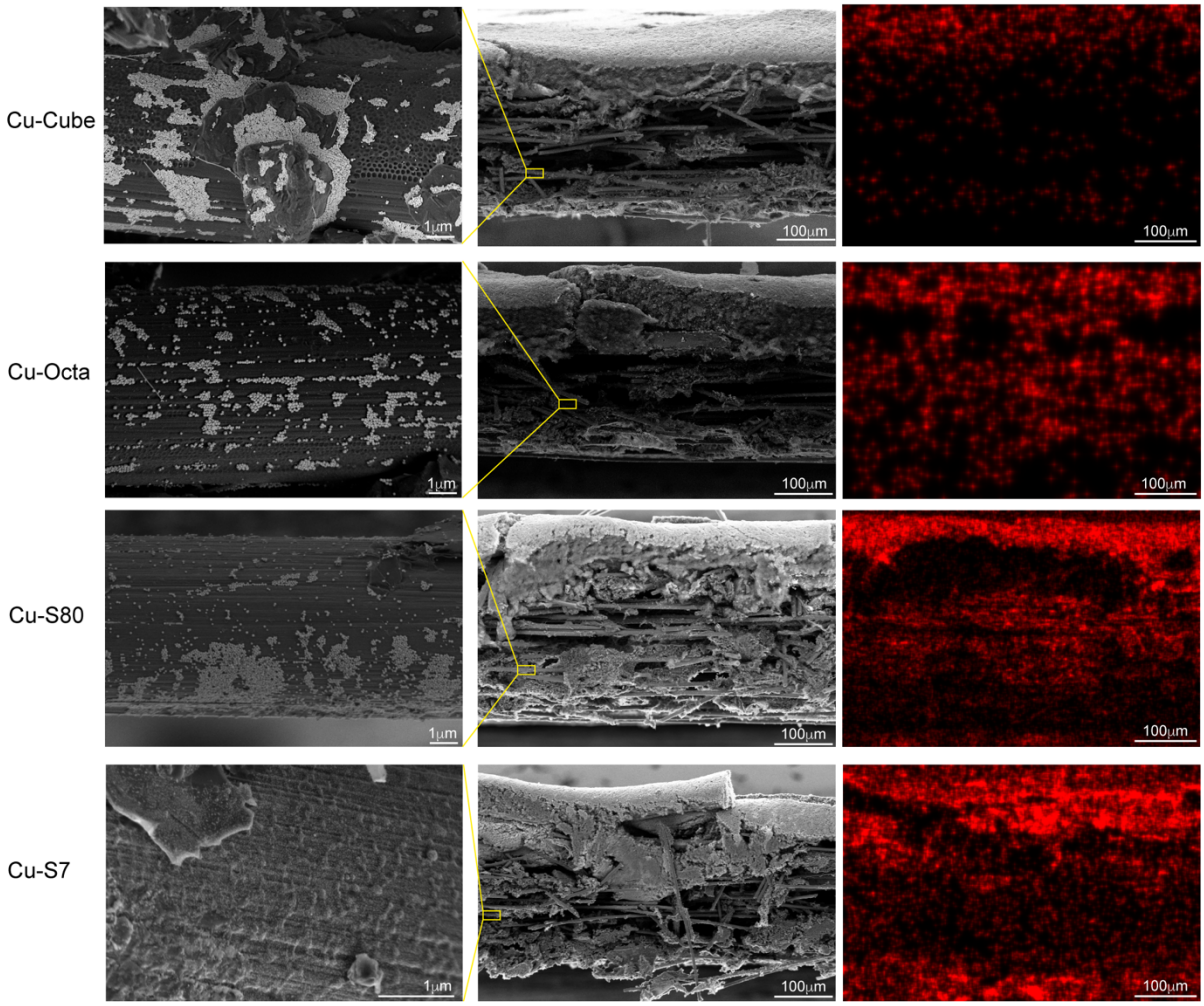

Supplementary Fig. 9 Cross-sectional SEM images of Cu-Octa, Cu-Cube, Cu-S80 and Cu-S7 together with the corresponding Cu EDX maps and a zoomed area showing that all the NCs penetrate through the entire GDL. Thus, major transport differences should not be involved in determining the performance of these electrodes. The loading for all catalysts was kept constant to 100 μg/cm^2.

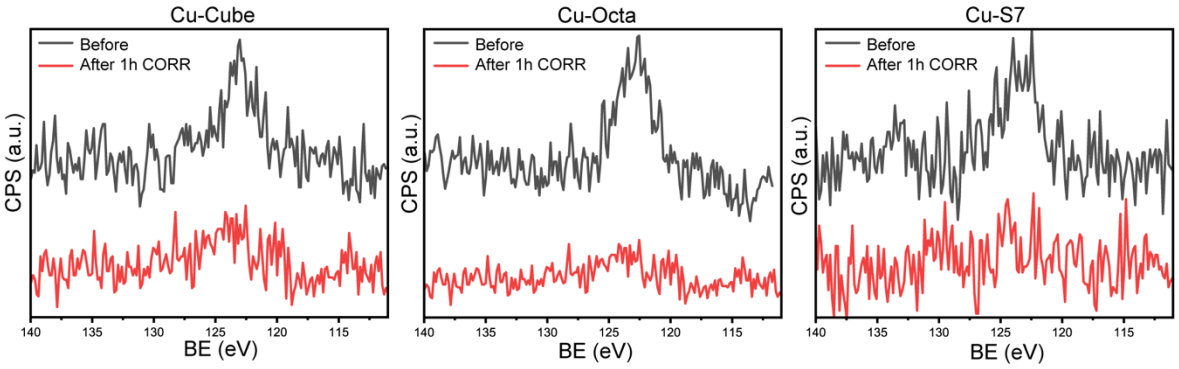

Supplementary Fig. 10 XPS of P 2p core level for Cu-Cube, Cu-Octa and Cu-S7 showing that no residual ligands on the surface after 1 h CORR.

The data above indicate that all ligands are electrochemically stripped, which is consistent with previous observations.[12] Thus, we do not expect any major impact on the catalytic behavior.

Additional computational details

Structural models: Three shape nanoparticles are generated from Cu fcc bulk, covering sizes of 2.53, 5.07 and 7.60 nm. The cube nanoparticles were built by isolating the supercell of the fcc bulk by 15 Å vacuum in all three directions. The spherical nanoparticles were built by deleting the atom outside the radius and 15 Å vacuum is applied in all three directions. The octahedra nanoparticles were built using the Wulff construction in ASE[13] with the surface energy of (100), (110), and (111) from experiment.[14] To simulate the defect in the nanoparticle, 5% of the surface or 5% of all the atoms are randomly removed, respectively. In addition, to model potential oxidation of the materials, 5% of the surface or 5% of all the atoms were replaced by oxygen, respectively.

NN-MD simulations: The simulations using our Neural Network potential[15] based Molecular Dynamics (NN-MD) were performed by means of LAMMPS code[16] with the NN interface from n2p2.[18,17] The potential was trained using database including Cu, Cu_2O, and Cu_xO with 59,491 points containing 1,801,491 atomic environments. The potential was validated for Cu based slab and cluster systems. For equilibrations, the NN-MDs were run for 100 ps at 300 K, with steps of 0.3 ps) in the canonical ensemble (NVT) using our constructed Behler-Parrinello-type HDNNP.[15,19] The simulations in NVT ensemble were modelled with the Nosé–Hoover thermostat. The simulation reaches equilibration as the coordination number converges after 1 ps (3 steps of 0.3 ps). To avoid electronic structure embedding instabilities, the models of adclusters adsorbed on the metal slab are relaxed using the neural-network potential with the adcluster fixed and the metal slab relaxed. The relaxations were stopped when the residual forces are below 0.03 eV/Å.

Strain analysis: To characterize the differences between studied sizes and shapes, the analysis of coordination numbers and strain of all the surface atoms of each NCs was carried out. First,

to identify the surface atoms a surface mesh was constructed using the alpha-shape method[20] implemented in OVITO[21] software. For strain analysis, atoms within a 3.05 Å distance were considered and strain was obtained as a percentage of deformation using Equation S1.

$$\text{Strain (\%)} = \frac{\sum_{l=1}^{L}\sum_{s=1}^{S}\sum_{n=1}^{N_{l,s}}(|d_{n,l,s} - d_{\text{Cu-Cu}}|/d_{\text{Cu-Cu}})/N_{l,s}}{S \cdot L} \cdot 100 \qquad \text{(Eq. S1)}$$

Where L is the number of NN-MD timesteps (334 steps), S is the number of surface atoms, $N_{l,s}$ is the number of neighboring Cu atoms (within 3.05 Å) of surface atom s at step l, $d_{n,l,s}$ is the distance between neighboring atom n and surface atom s at step l, and $d_{\text{Cu-Cu}}$ is the Cu-Cu bulk distance (2.57 Å).

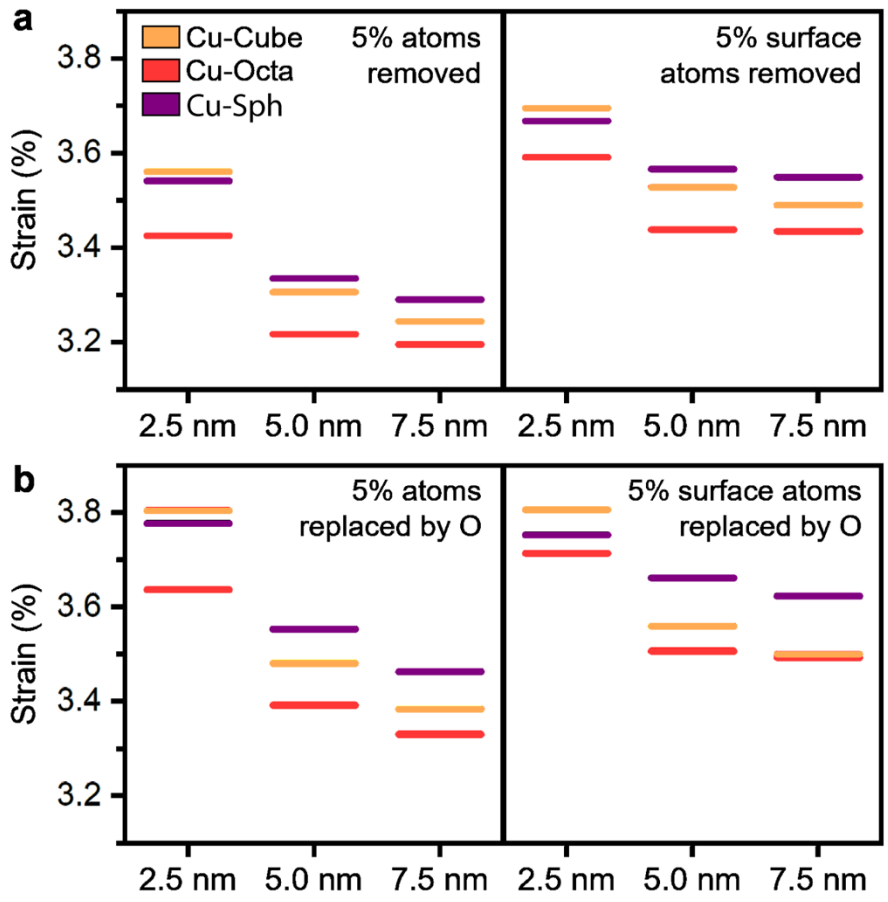

Supplementary Fig. 11 Average strain of NCs models along all 334 NN-MD steps (a) with 5% of total Cu atoms and surface Cu atoms removed and (b) with 5% of total Cu atoms and surface Cu atoms replaced by O atoms.

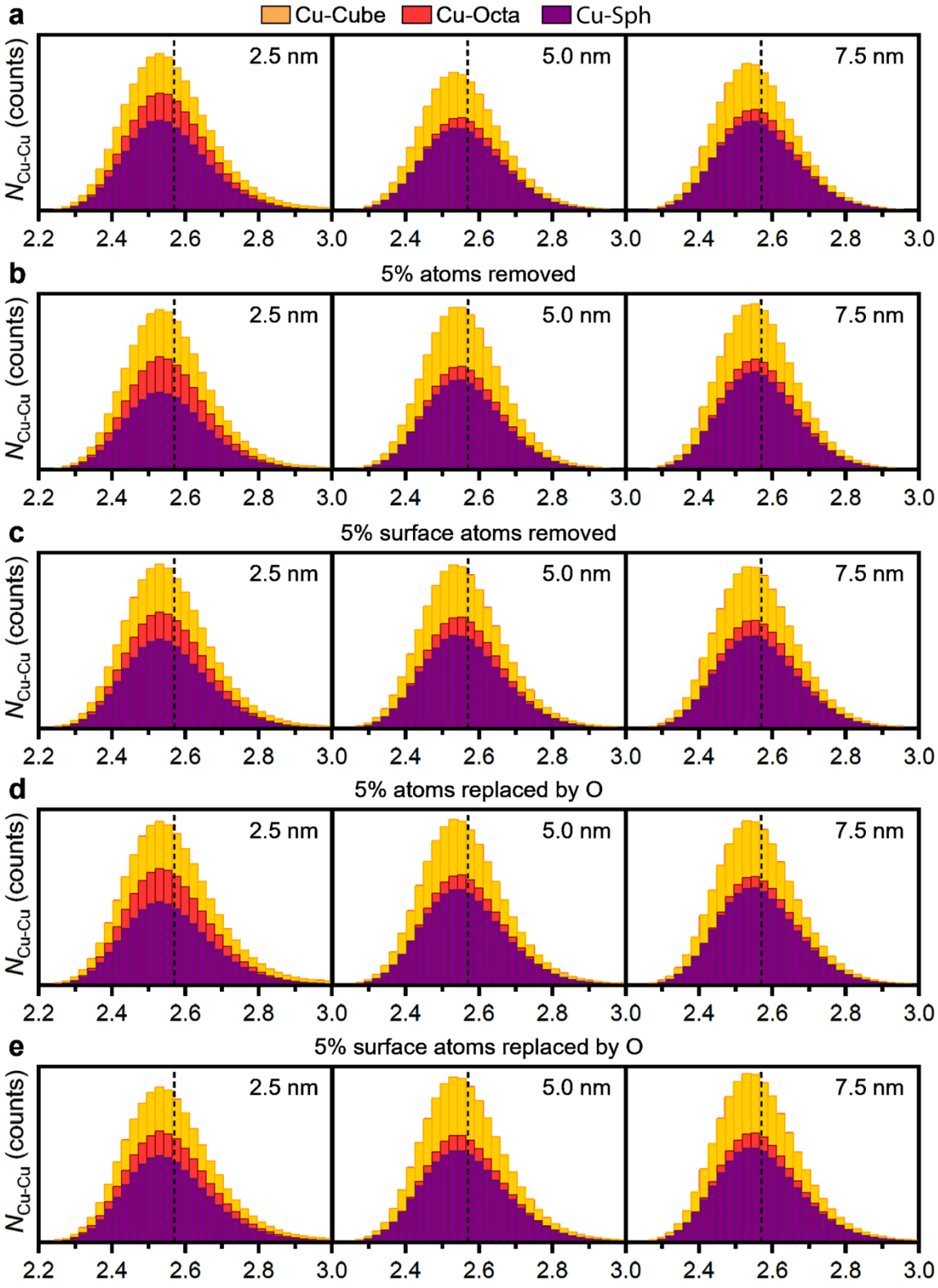

Supplementary Fig. 12 Histogram of Cu-Cu bond length for (a) metallic Cu NCs models (b) models with 5% of total Cu atoms removed (c) models with 5% of surface Cu atoms removed (d) models with 5% of total Cu atoms replaced by O atoms (e) models with 5% of surface Cu atoms replaced by O atoms. Distances are averaged along the 334 NN-MD steps.

Supplementary Note 2: Identification of active site models in Cu spheres for DFT calculation

Coordination Number (CN) analysis: To identify the unique active sites in sphere NCs, CN analysis was carried out for all models taking as center each surface atom and counting the number of neighboring atoms within 2.7 Å. For each of the NN-MD step, the population (in %) of atoms with each CN were obtained, and the average within the 334 steps was reported as total CN population. While for all 3 sizes cube showed the highest amount of CN = 8 atoms (33-41%) normally associated with Cu(100) facets, octahedra showed the highest population of CN = 9 (12-22%) on its surface which agrees with the expected exposure of Cu(111) (**Supplementary Fig. 13**). Although the population of low-coordinated atoms (CN < 8) was similar for all 3 shapes, spheres showed an increase of CN = 6 atoms compared to cube and octahedra and a decrease of CN = 7 atoms (normally associated to Cu(211)-like step sites). Same trends were observed for the models including partial removal of Cu atoms and partial substitution by O atoms (**Supplementary Figs. S14-17**). Therefore, we considered these sites identified by Cu surface atoms with CN = 6 to be the unique active sites present in sphere NCs.

Generation of active sites structures: For each studied size of sphere NCs (2.5, 5.0 and 7.5 nm as diameter) 10 active sites with CN = 6 were selected for studying their reactivity, for a total of 30 structures. Atoms which have CN of 6 during more than 75% of the NN-MD steps were considered as 6-coordinated Cu atoms active sites. However, the large sizes of structures obtained from the dynamics hindered the reactivity study using explicit DFT, thus these sites of interest were cut from the final structure of each NN-MD. A 12x12 $Å^2$ plane centered on the selected atom with the normal vector pointing to the center of the NC was used, and from this plane 6 Å depth structures were taken for reactivity study. Among all structures resulting from atoms with CN = 6, we selected 30 structures with different strain values ranging from 1.92 to

5.42 % to also evaluate the effect of this property on stability of intermediates. To avoid electronic structure embedding problems, all the adclusters were embedded on top of Cu(100) and Cu(111) (4x4) and (3x3) 3 layer surfaces. As a minimum number of 5 atoms in the bottom layer of the adcluster (within 0.2 Å from lowest atom) is required to ensure a proper placing on top of the flat surface, some structures were polished by removing the lowest atom one by one since this minimum number of atoms is achieved. Adclusters were placed at the regular interlayer distance of both (100) and (111) surfaces (1.8177 and 2.099 Å, respectively). Then, for each slab 3 different approaches were benchmarked: fixing the whole structure and optimizing the adcluster-surface interface using NN structural optimization (with forces smaller than 0.03 eV/Å as convergence criterium) with the active ensemble fixed or the overall adcluster fixed. Finaly, the resulting slabs were evaluated as descriptors of active sites using as indicators of proper electronic convergence the Fermi energy (ε_{Fermi}) and the CO adsorption energy (ΔE_{*CO}), **Supplementary Figs. 17,18**. Adclusters cut in smaller size (10x10x5 $Å^3$ instead of 12x12x6 $Å^3$) were also benchmarked, resulting in a higher difference of ε_{Fermi} compared with Cu(100) and Cu(111) slabs. Moreover, the ones placed in Cu(100) surface and further optimized with the whole adcluster fixed were the ones showing the narrowest distribution of Fermi energies and ΔE_{*CO}. (**Supplementary Figs. 18,19**). Thus, it was used as the strategy to build the active site models for the reactivity study by means of DFT adsorption energy of key intermediates.

Energy of intermediates: Potential energies of reaction intermediates were obtained using CO_2, H_2O, and H_2/H^+ as thermodynamic sinks (Equations S2-S4).

$$xCO_2 + * + (z-2x)H_2O + (4x+y-2z)H^+ + (4x+y-2z)e^- \rightarrow {}^*C_xH_yO_z \quad \text{(Eq. S2)}$$

$$E_{*C_xH_yO_z} = E_{DFT,*C_xH_yO_z} - E_* - (x)E_{CO_2} - (z-2x)E_{H_2O} - (4x+y-2z)E_{H^+} + n_{e^-}U \quad \text{(Eq. S3)}$$

$$n_{e^-} = (4x+y-2z) \quad \text{(Eq. S4)}$$

The Computational Hydrogen Electrode (CHE)[22,23] was used to obtain the relative energy of H^+ from gas phase H_2 computed energy at $U = 0$ V_{RHE}, Equation S5.

$$E_{H^+} = \frac{1}{2} E_{H_2} \qquad \text{(Eq. S5)}$$

Only in the case of *CO adsorption energies used for benchmarking the active sites structures (see **Supplementary Fig. 19**), gas phase CO energy was used as the unique thermodynamic sink.

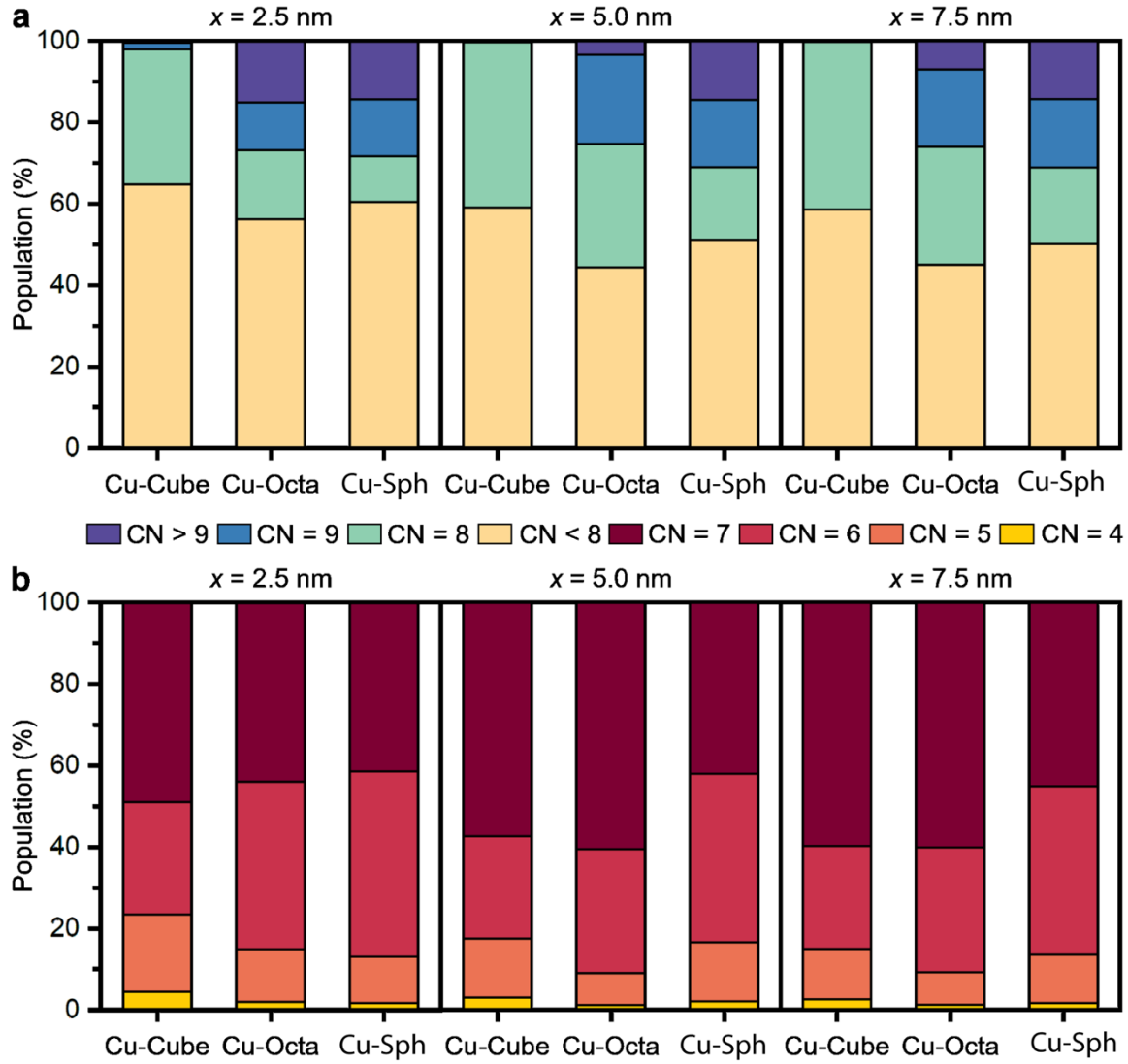

Supplementary Fig. 13 Coordination number (CN) population averaged along all 334 NN-MD steps of (a) total surface Cu atoms and (b) low-coordination (CN < 8) surface Cu atoms for metallic Cu NCs models.

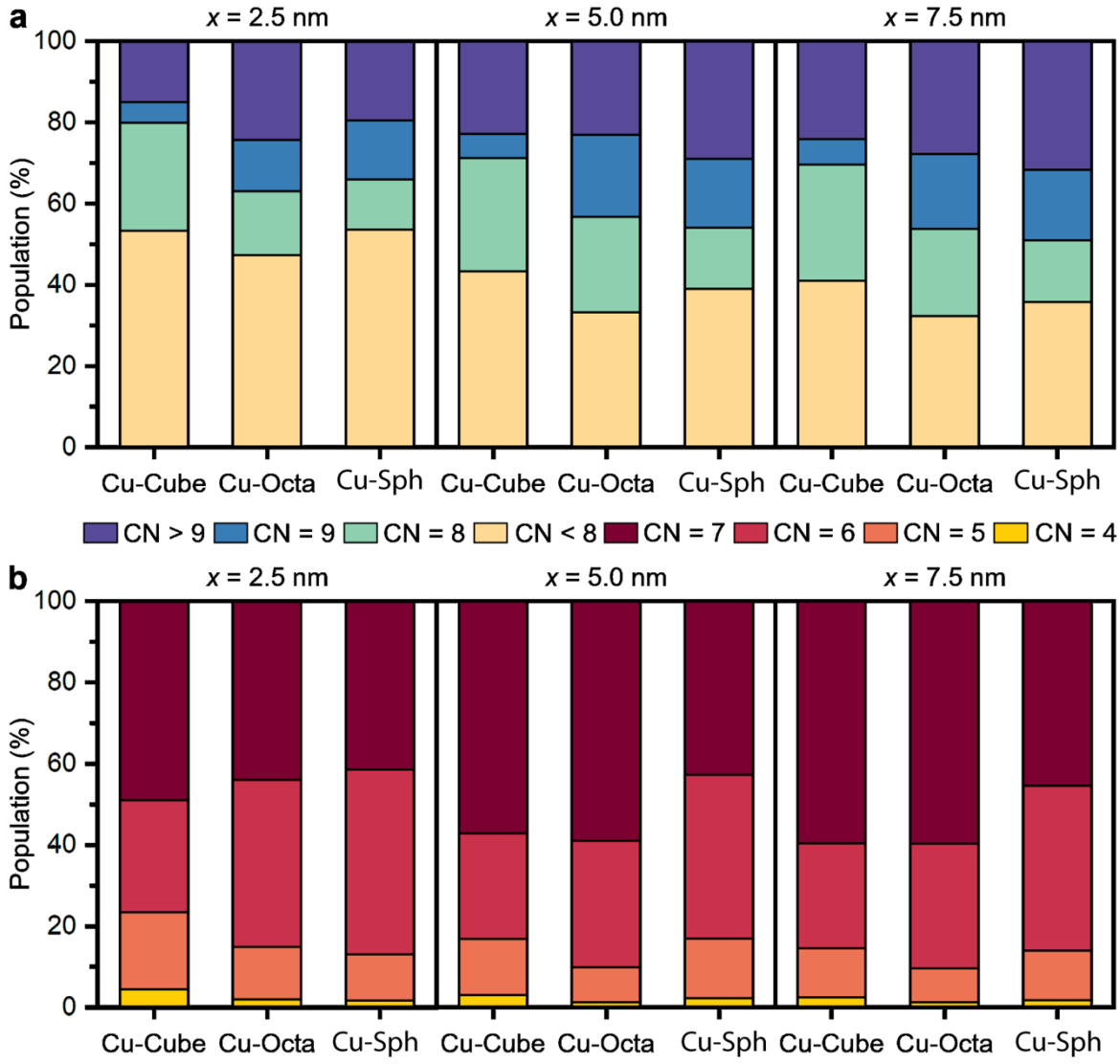

Supplementary Fig. 14 Coordination number (CN) population averaged along all 334 NN-MD steps of (a) total surface Cu atoms and (b) low-coordination (CN < 8) surface Cu atoms for models with 5% of total Cu atoms removed.

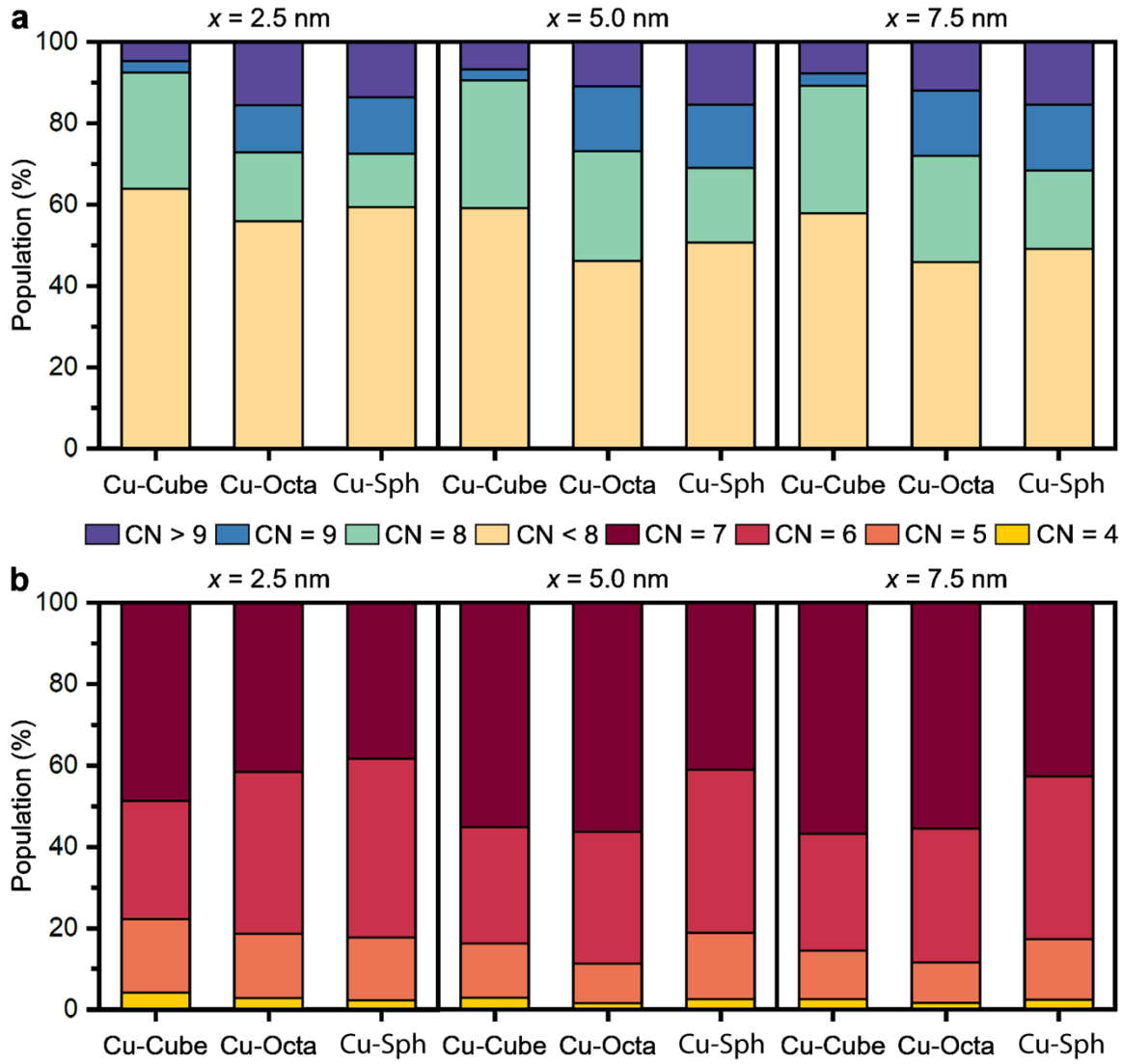

Supplementary Fig. 15 Coordination number (CN) population averaged along all 334 NN-MD steps of (a) total surface Cu atoms and (b) low-coordination (CN < 8) surface Cu atoms for models with 5% of surface Cu atoms removed.

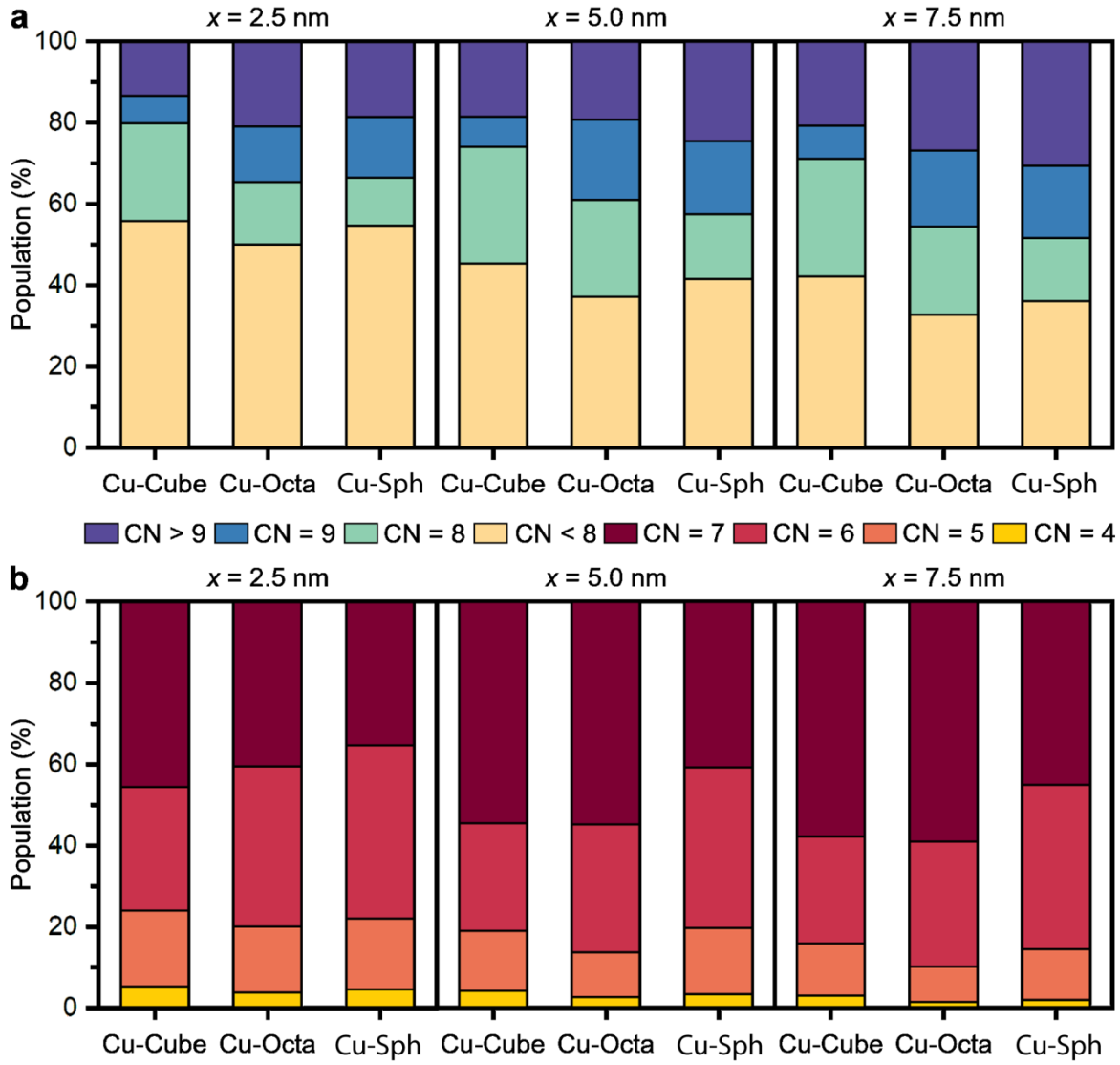

Supplementary Fig. 16 Coordination number (CN) population averaged along all 334 NN-MD steps of (a) total surface Cu atoms and (b) low-coordination (CN < 8) surface Cu atoms for models with 5% of total Cu atoms replaced by O atoms.

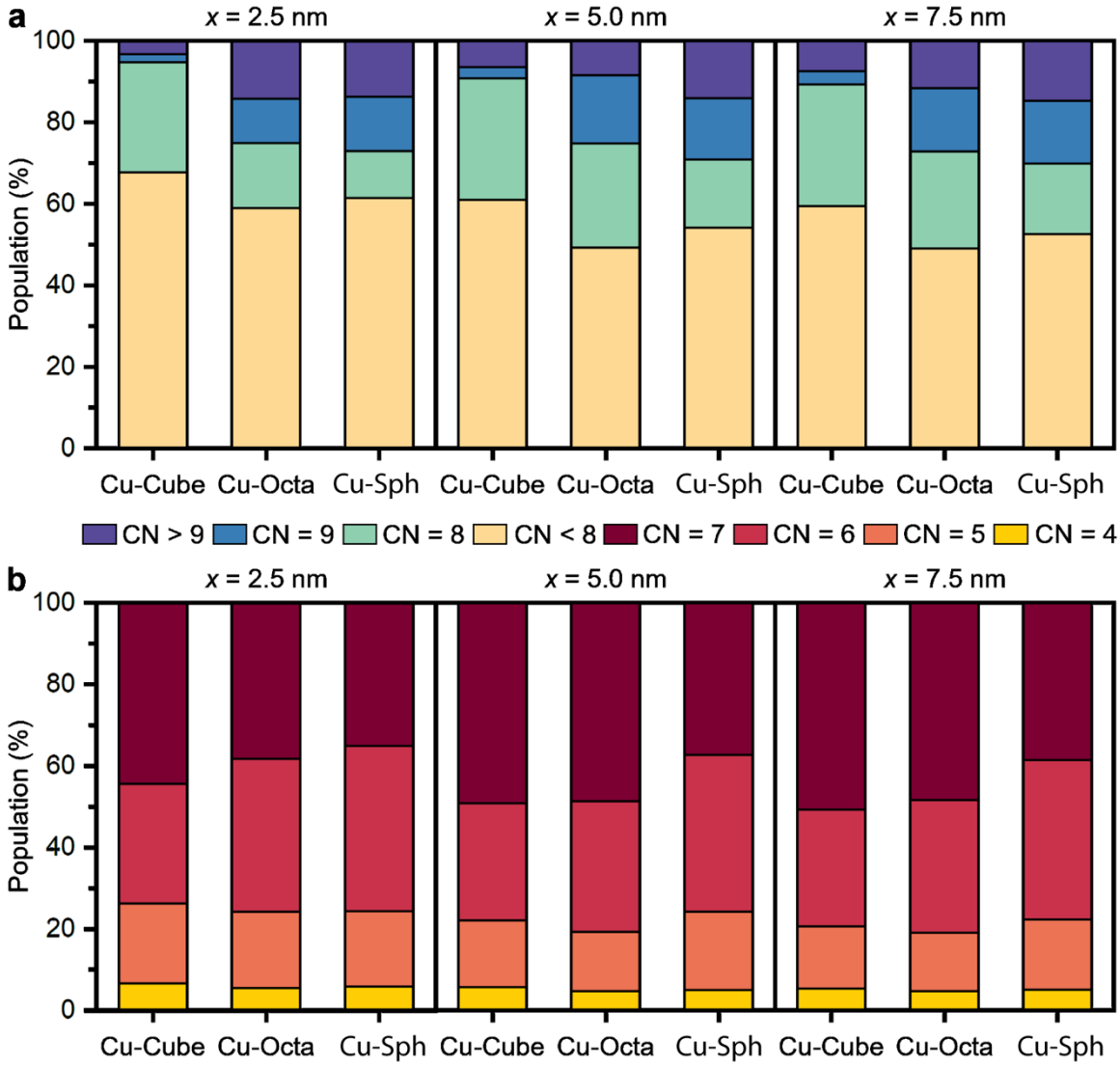

Supplementary Fig. 17 Coordination number (CN) population averaged along all 334 NN-MD steps of (a) total surface Cu atoms and (b) low-coordination (CN < 8) surface Cu atoms for models with 5% of surface Cu atoms replaced by O atoms.

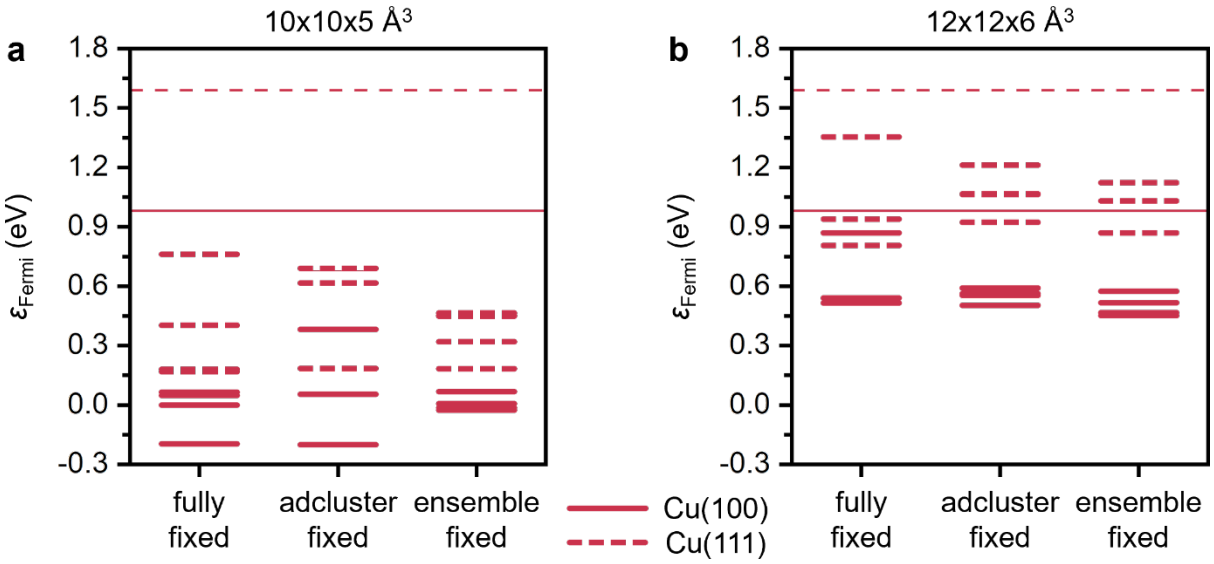

Supplementary Fig. 18 Benchmarking of different optimization techniques for the construction of active sites by placing on Cu(100) and Cu(111) periodic slab the extracted local environment of the active site with a size of (a) 10x10x5 Å^3 and (b) 12x12x6 Å^3. Electronic convergence is evaluated in terms of Fermi energy by comparing them with Cu(111) and Cu(100) values.

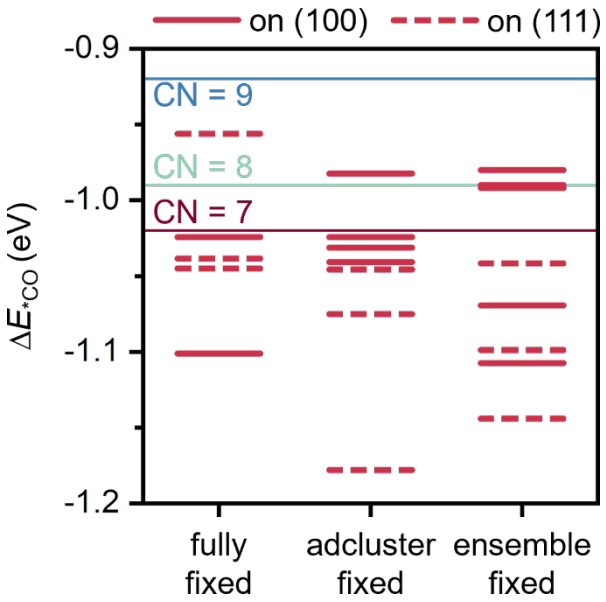

Supplementary Fig. 19 Benchmarking of different optimization techniques for the construction of active sites by placing on Cu(100) and Cu(111) periodic slab the extracted local environment of the active site with a size of 12x12x6 Å^3. CO adsorption energies are evaluated by comparing them with Cu(111), Cu(100), and Cu(211) values (CN = 9, 8, and 7, respectively).

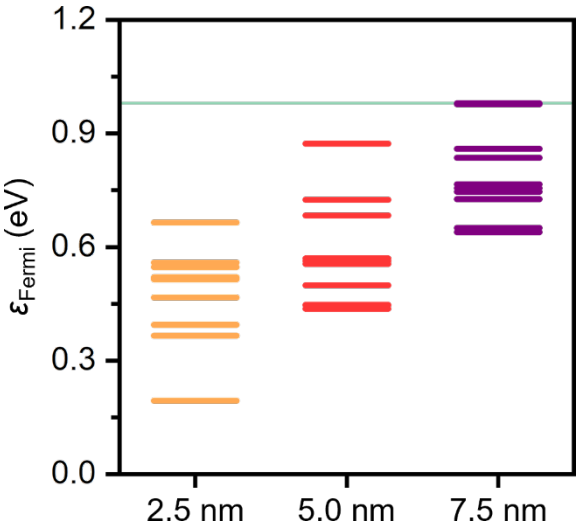

Supplementary Fig. 20 Fermi energies of 30 selected, extracted, and reconstructed active sites for reactivity study. Green line represents the Fermi energy of Cu(100) surface for comparison.

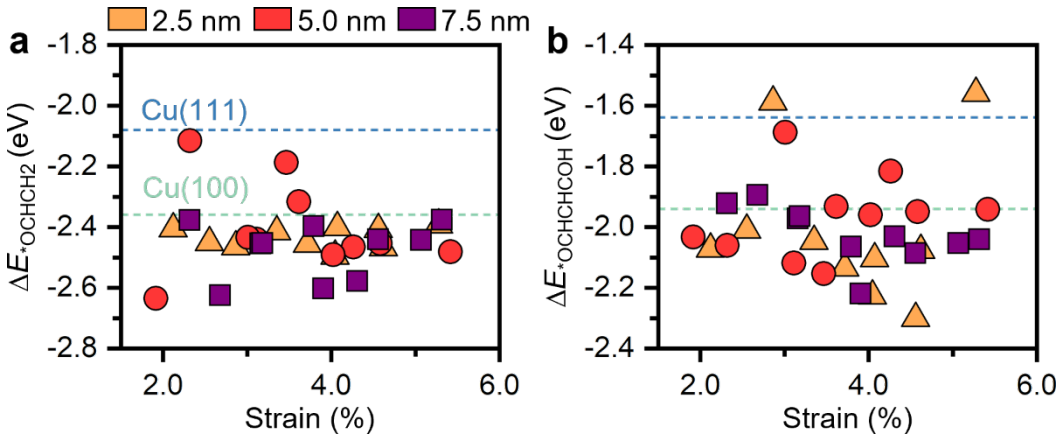

Supplementary Fig. 21 Adsorption energies of (a) *$OCHCH_2$ and (b) *OCHCHCOH intermediates in the 30 studied active sites as a function of site local strain.

Supplementary Table 3. Local strain values for the database of 30 active sites (10 extracted from each sphere model size) used for DFT reactivity study.

	Strain (%)		
Active site ID	**2.5 nm**	**5.0 nm**	**7.5 nm**
1	4.56	4.58	3.79
2	4.62	2.32	3.16
3	3.35	1.92	2.32
4	4.04	5.42	4.55
5	4.07	4.26	3.90
6	3.72	3.47	5.07
7	5.28	3.61	4.31
8	2.87	3.11	5.31
9	2.55	4.02	3.18
10	2.12	3.01	2.68

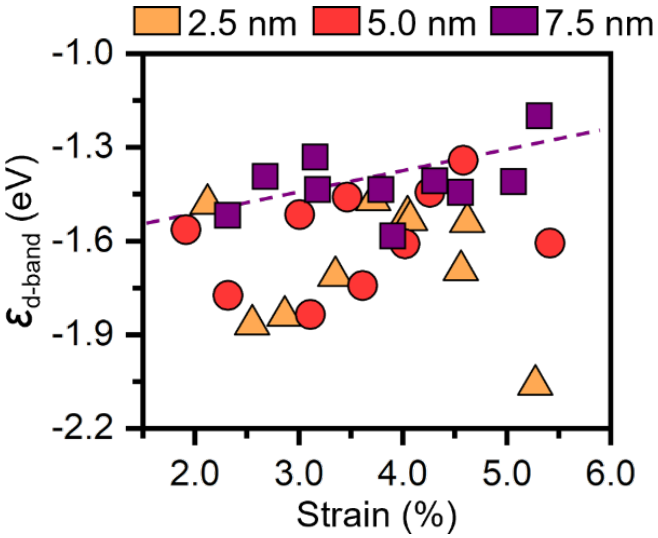

Supplementary Fig. 22 d-band center energies of each active site structure as a function of its local strain. Purple dashed line is used to guide the eye.

Supplementary Note 3: Strain investigation in Cu NC ex-situ and during CORR

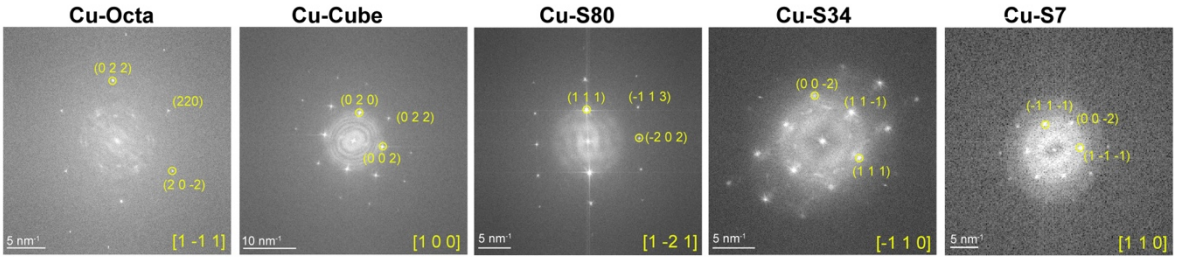

Supplementary Fig. 23 FFT images corresponding to the HRTEM images in Fig. 3a. The yellow circles are the spots used for the GPA analysis.

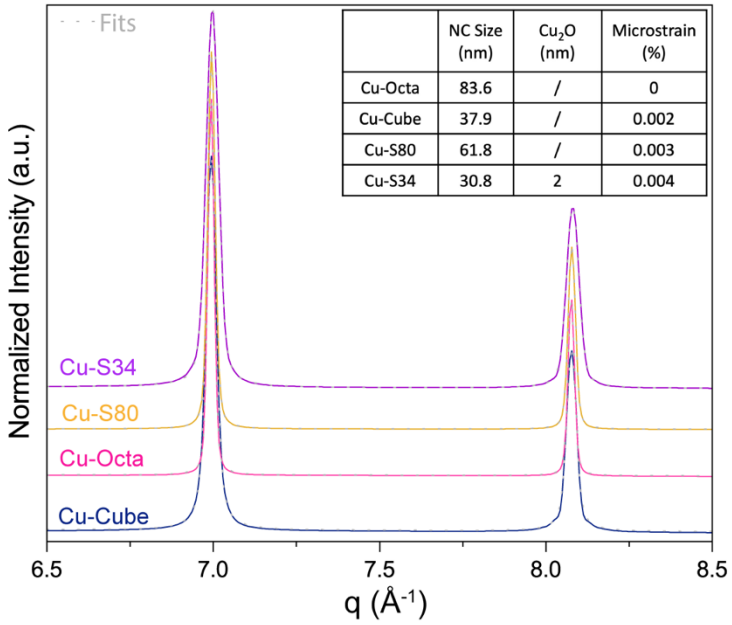

	NC Size (nm)	Cu_2O (nm)	Microstrain (%)
Cu-Octa	83.6	/	0
Cu-Cube	37.9	/	0.002
Cu-S80	61.8	/	0.003
Cu-S34	30.8	2	0.004

Supplementary Fig. 24 Ex-situ XRD data of the as-prepared Cu-Cube, Cu-Octa, Cu-S80 and Cu-S34. The table reports the extracted corresponding NC size and strain from the fitting.

The microstrain % decreases from Cu-Octa < Cu-cube < Cu-S80 < Cu-S34. We note that the size of the NCs studied is relatively large, so the "bulk" contribution hinders eventual surface strain effects. Cu-S7 was too small to obtained an optimal signal-to-noise ratio for strain analysis.

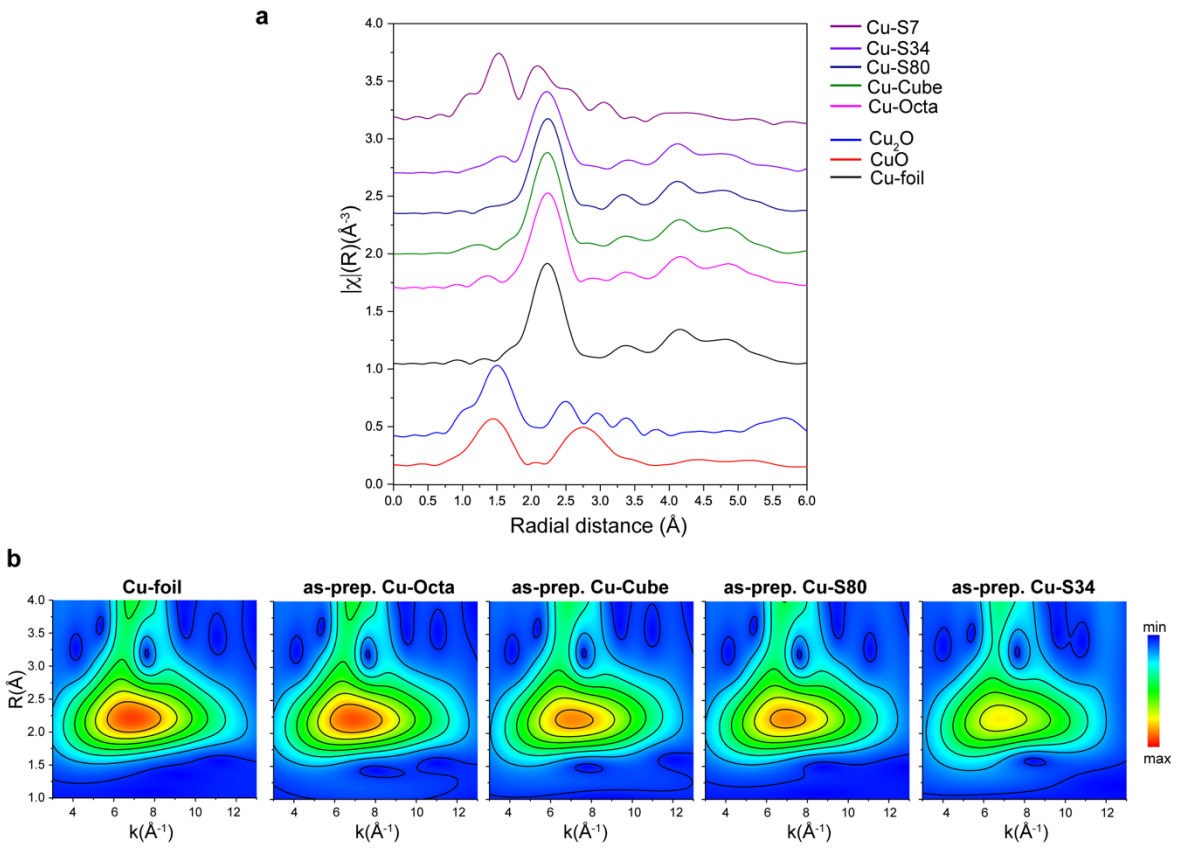

Supplementary Fig. 25 a, FT(k^3)-EXAFS plots for as-prepared Cu-Octa, Cu-Cube, Cu-S80, Cu-S34 and Cu-S7. The intensity was scaled of a 0.25 factor to better compare them. **b,** k-R Wavelet transformed-EXAFS (WT-EXAFS) contour maps for Cu-Cube, Cu-Octa, Cu-S80 and Cu-S34 where the intensity has been set to the same scale for all samples. WT-EXAFS data are not phase corrected.

For the as-prepared samples, we observed a similar trend of the OCP samples showed in **Supplementary Fig. 5**. The fraction of oxidized copper species increases as the surface-to-volume ratio increases, with the Cu-S7 showing the highest degree of oxidation.

The WT-EXAFS contour maps of the as prepared samples denote the same trend observed during operation (**Fig. 3e** of the manuscript), which is a decrease in intensity and broadening of the signal going from Cu-Octa to Cu-Cube, Cu-S80 and Cu-S34. A closer look indicates a shift of the maximum (i.e. change in the Cu-Cu bond length).

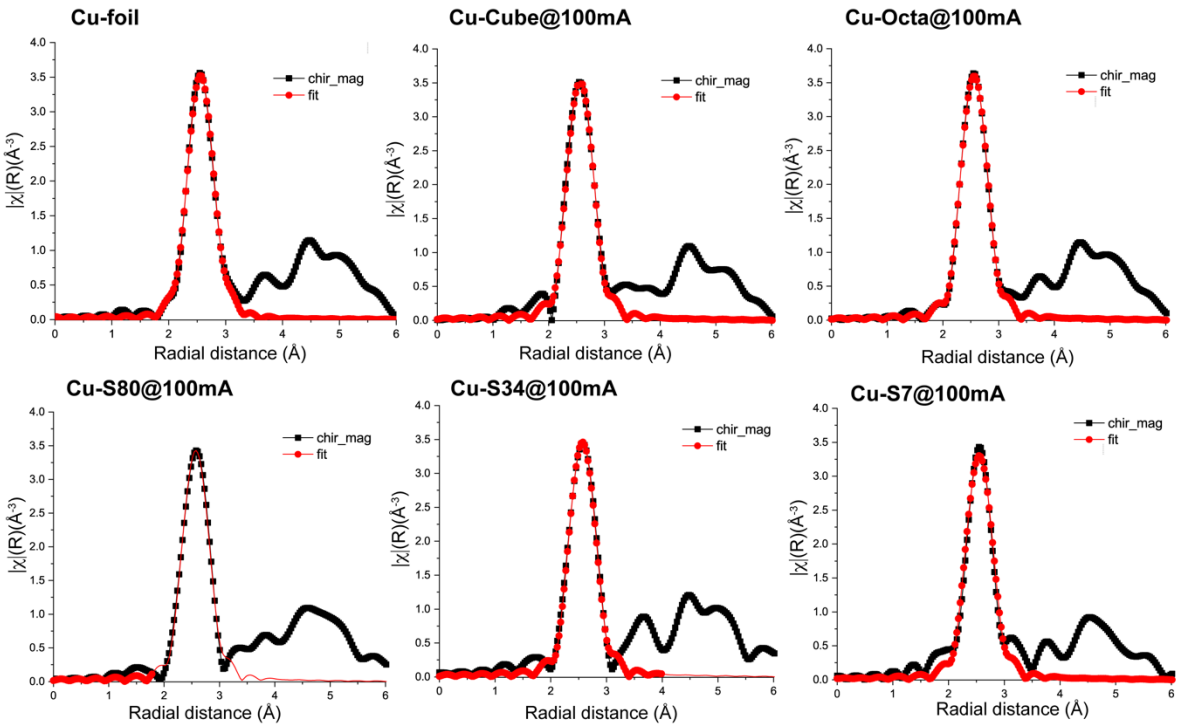

Supplementary Fig. 26 Phase-corrected FT(k^3)-EXAFS spectra at 100 mA/cm^2 (black) with their respective fittings (red) of Cu-foil, Cu-Cube, Cu-Octa, Cu-S80, Cu-S34 and Cu-S7.

In all cases the fitted data range is $3 \leq k\ (Å^{-1}) \leq 12$ and the fitting made using a k^3 weighting of the EXAFS data.

Supplementary Table 4. Structural data extracted from analysis of Cu K-edge EXAFS of the tested samples at 100 mA/cm^2 in 0.5 M KOH and Cu-foil. The data are all referred to Cu-Cu bond.

Sample	CN	R (Å)	R_{eff}	E_0	DWF	R-factor
Cu-foil	12.00	2.541±0.004	2.56	4.09	0.0085	0.0036
Cu-Cube	11.67±1.46	2.541±0.008		4.95	0.0080	0.0122
Cu-Octa	11.81±0.85	2.540±0.005		4.49	0.0080	0.0034
Cu-S80	11.74±1.28	2.545±0.007		5.24	0.0083	0.0101
Cu-S34	11.20±1.13	2.545±0.007		4.89	0.0078	0.0081
Cu-S7	11.12±2.08	2.533±0.010		4.21	0.0083	0.0183

CN: coordination number, R: bond length, R_{eff}: Cu-Cu bond length of bulk, E_0: energy shift, DWF: Debye-Waller factor, R-factor: it is a measure of the percentage of misfit between the measured data and the calculated (theoretical) pattern. The s_0^2 factor extracted from the Cu-foil was of 0.857. This value was kept fixed during the fitting for reducing the number of fitted parameters.

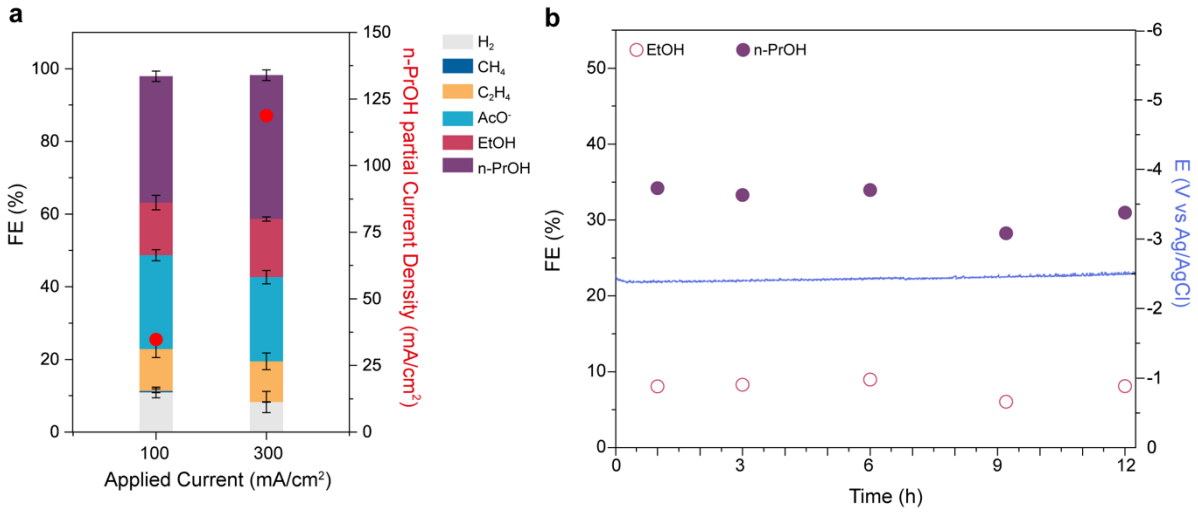

Supplementary Fig. 27. a, Total FEs for CORR at 100 mA/cm^2 and 300 mA/cm^2 of Cu-S4 in 0.5 M KOH and 1 M KOH respectively. Loading is constant to 100 µg/cm^2. The reported values are an average of three independent experiments with error bars indicating the standard deviations. **b,** n-PrOH FE and corresponding measured half-cell potential over 12 hours at a constant current of 100 mA/cm^2 in 0.5 M KOH.

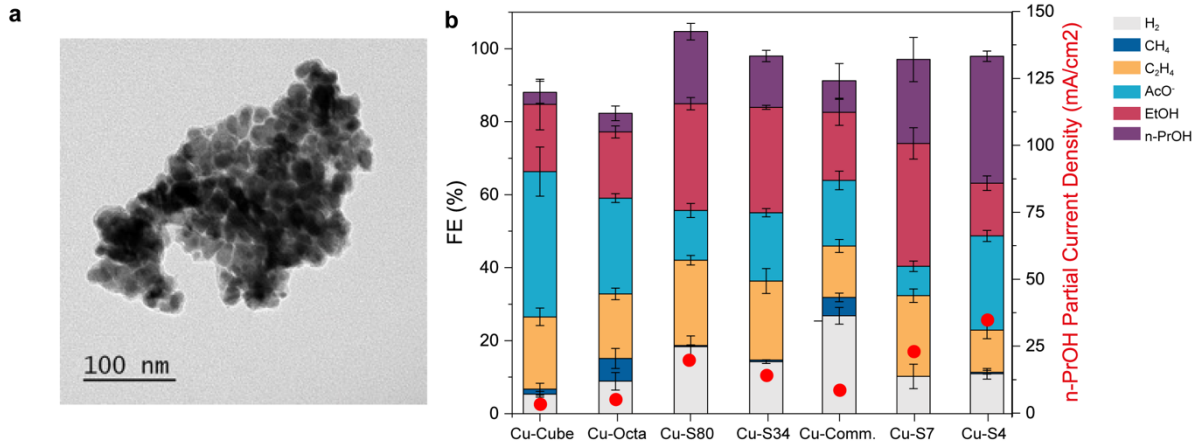

Supplementary Fig. 28. a, TEM image of commercial Cu NCs (Cu-Comm.) and **b,** the total FEs for CORR in 0.5 M KOH at 100 mA/cm^2 of Cu-Comm. compared with all the other Cu tested in this work at the same loading of 100 µg/cm^2. The reported values are an average of three independent experiments with error bars indicating the standard deviations.

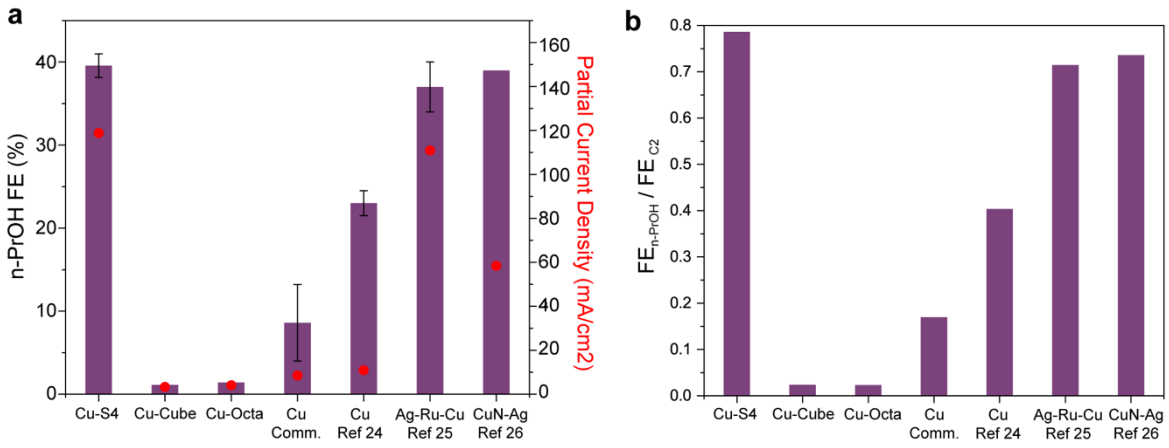

Supplementary Fig. 29: Comparison of FE performance with state-of-the-art Cu catalyst for n-PrOH from CO. a, FE and production rate for n-propanol in state-of-the-art catalysts for n-propanol from CORR compared with our studied Cu NCs.[24,25,26] **b**, Ratio of the faradaic efficiencies for n-PrOH FE and for C_2 of the same electrodes in **a**.

These data show that Cu-S4 outperform all the Cu catalysts reported so far both in selectivity and productivity for n-propanol. They show comparable performance with Cu catalysts co-doped with Ag and Ru both for selectivity and productivity.

Supplementary Table 5: All literature reports on n-Propanol electrosynthesis from CORR to date. The data relative to catalysts containing noble metals are shaded in gray.

Catalysts	**Electrolyte**	**J_{total} (mA/cm^2)**	**$FE_{n\text{-}PrOH}$ (%)**	**$J_{n\text{-}PrOH}$ (mA/cm^2)**	**References**
Oxide-derived Cu	0.1 M KOH, H-cell	<1	-	-	27
Cu nanowires	1.0 M KOH	< 1	6.2	-	28
Oxide-derived Cu	1.0 M KOH	1050	4.9	51.45	29
Cu adparticle	1.0 M KOH	~50	23.1	11	24
Cu nanocavities	1.0 M KOH	100	12	13	30
Fragmented Cu	1.0 M KOH	43	20.3	8.5	10
Cu-S4	**1 M KOH**	**300**	**39.6**	**118.8**	**This work**
Ag-doped Cu	1.0 M KOH	~13	33.3	4.5	31
Ag-Ru doped Cu	1.0 M KOH	300	37	111	25
$CuAg_{5\%}N$	1 M KOH	150	39	58.5	26
$CuAg_{5\%}N$	1 M CsOH	150	45	67.5	26
CuAg alloy* (high pressure)	1 M $CsHCO_3$	300	56.7	59.3	32
CuAg alloy* (atm. pressure)	1 M $CsHCO_3$	-	39.6	12.03	32

*This refers to the state-of-the-art n-PrOH performance obtained from CO_2RR using high-pressure (10 bar) or atmospheric pressure electrochemical cell.

References

[1] Strach, M. et al. Insights into Reaction Intermediates to Predict Synthetic Pathways for Shape-Controlled Metal Nanocrystals. *J. Am. Chem. Soc.* **141**, 41, 16312–16322 (2019).

[2] Mantella, V. et al. Polymer lamellae as reaction intermediates in the formation of copper nanospheres as evidenced by in situ X-ray studies. *Angew. Int. Chem. Ed. Engl.* **59**, 11627–11633 (2020).

[3] Wu, Y. et al. Mitigating Electrolyte Flooding for Electrochemical CO2 Reduction via Infiltration of Hydrophobic Particles in a Gas Diffusion Layer. *ACS Energy Letters* **7** (9), 2884-2892 (2022).

[4] De Gregorio, G.L., Burdyny, T., Loiudice, A., Iyengar, P., Smith, W.A. & Buonsanti**,** R. Facet-Dependent Selectivity of Cu Catalysts in Electrochemical CO_2 Reduction at Commercially Viable Current Densities. *ACS Catalysis* **10** (9), 4854-4862 (2020).

[5] Ma, M., Clark, E. L., Dalsgaard, S., Therkildsen, K. T., Chorkendorff, I. & Seger, B. J. Insights into the Carbon Balance for CO_2 Electroreduction on Cu using Gas Diffusion Electrode Reactor Designs. *Energy Environ. Sci.* **13**, 977, (2020).

[6] Jin, J., Wicks, J., Min, Q. et al. Constrained C2 adsorbate orientation enables CO-to-acetate electroreduction. Nature **617**, 724–729 (2023).

[7] Luc, W., Fu, X., Shi, J. et al. Two-dimensional copper nanosheets for electrochemical reduction of carbon monoxide to acetate. *Nat Catal* **2**, 423–430 (2019).

[8] Bertheussen, E. et al. Acetaldehyde as an Intermediate in the Electroreduction of Carbon Monoxide to Ethanol on Oxide-Derived Copper. *Angew. Chem. Int. Ed.* **55**, 1450 –1454, (2016).

[9] Qiao, Y., Hochfilzer, D., Kibsgaard, J., Chorkendorff, I. & Seger, B. Real-Time Detection of Acetaldehyde in Electrochemical CO Reduction on Cu Single Crystals. *ACS Energy Letters* **9** (3), 880-887, (2024).

[10] Pang, Y., Li, J., Wang, Z. *et al.* Efficient electrocatalytic conversion of carbon monoxide to propanol using fragmented copper. *Nat Catal* **2**, 251–258 (2019).

[11] Albertini, P.P., Newton, M.A., Wang, M. *et al.* Hybrid oxide coatings generate stable Cu catalysts for CO_2 electroreduction. *Nat. Mater.* **23**, 680–687 (2024).

[12] Pankhurst, J. R., Iyengar, P., Loiudice, A., Mensi, M. & Buonsanti, R. Metal–ligand bond strength determines the fate of organic ligands on the catalyst surface during the electrochemical CO2 reduction reaction. *Chem. Sci.*, **11**, 9296-9302, (2020).

[13] Larsen, A.H. et al. The atomic simulation environment—a Python library for working with atoms. *J. Phys.: Condens. Matter* **29** 273002, (2017).

[14] L. Vitos, L., Ruban, A.V., Skriver, H.L. & Kollár, J. The surface energy of metals. *Surf. Sci.* **422**, 1-2, 186-202, (1988).

[15] Lian, Z., Dattila, F. & López, N. Stability and lifetime of diffusion-trapped oxygen in oxide-derived copper CO_2 reduction electrocatalysts. *Nat Catal* **7**, 401–411 (2024).

[16] Thomspson, A. et al. LAMMPS - a flexible simulation tool for particle-based materials modeling at the atomic, meso, and continuum scales. *Comput. Phys. Comm.* **271**, 108171 (2022).

[17] Singraber, A., Morawietz, T., Behler, J. & Christoph Dellago, C. Parallel Multistream Training of High-Dimensional Neural Network Potentials. *J. Chem. Theory Comput.* **15**, 5, 3075–3092 (2019).

[18] Singraber, A., Morawietz, T., Behler, J. & Christoph Dellago, C. Library-Based LAMMPS Implementation of High-Dimensional Neural Network Potentials. *J. Chem. Theory Comput.* **15**, 3, 1827–1840 (2019).

[19] Behler, J. Atom-centered symmetry functions for constructing high-dimensional neural network potentials. *J. Chem. Phys.* **134**, 074106 (2011).

[20] Stukowski, A. Computational Analysis Methods in Atomistic Modeling of Crystals. *JOM* **66**, 399–407 (2014).

[21] Stukowski, A. Visualization and analysis of atomistic simulation data with OVITO–the Open Visualization Tool. *Modelling Simul. Mater. Sci. Eng.* **18** 015012, (2010).

[22] Nørskov, J.K., Rossmeisl, J., Logadottir, A., Lindqvist, L., Kitchin, J.R., Bligaard, T. & Jónsson, H. Origin of the Overpotential for Oxygen Reduction at a Fuel-Cell Cathode. *J. Phys. Chem. B* **108**, 46, 17886–17892, (2004).

[23] Peterson, A.A., Abild-Pedersen, F., Studt, F., Rossmeisla, J. & Nørskov, J.K. How copper catalyzes the electroreduction of carbon dioxide into hydrocarbon fuels. *Energy Environ. Sci.* **3**, 1311-1315, (2010).

[24] Li, J., Che, F., Pang, Y. *et al.* Copper adparticle enabled selective electrosynthesis of n-propanol. *Nat Commun* **9**, 4614 (2018).

[25] Wang, X., Ou, P., Ozden, A. *et al.* Efficient electrosynthesis of *n*-propanol from carbon monoxide using a Ag–Ru–Cu catalyst. *Nat Energy* **7**, 170–176 (2022).

[26] Duong, H.P., Rivera de la Cruz, J.G., Tran, N.-H. *et al.* Silver and Copper Nitride Cooperate for CO Electroreduction to Propanol. *Angew. Chem. Int. Ed.* **62**, e202310788 (2023).

[27] Li, C., Ciston, J. & Kanan, M. Electroreduction of carbon monoxide to liquid fuel on oxide-derived nanocrystalline copper. *Nature* **508**, 504–507 (2014).

[28] Raciti, D. et al. Low-Overpotential Electroreduction of Carbon Monoxide Using Copper Nanowires. *ACS Catal.* **7**, 4467–4472 (2017).

[29] Jouny, M., Luc, W. & Jiao, F. High-rate electroreduction of carbon monoxide to multi-carbon products. *Nat. Catal.* **1**, 748-755 (2018).

[30] Zhuang, T.T., Pang, Y., Liang, Z.Q. *et al.* Copper nanocavities confine intermediates for efficient electrosynthesis of C_3 alcohol fuels from carbon monoxide. *Nat Catal* **1**, 946–951 (2018).

[31] Wang, X., Wang, Z., Zhuang, T.T. *et al.* Efficient upgrading of CO to C_3 fuel using asymmetric C-C coupling active sites. *Nat. Commun.* **10**, 5186 (2019).

[32] Qi, K., Zhang, Y., Onofrio, N. *et al.* Unlocking direct CO_2 electrolysis to C_3 products via electrolyte supersaturation. *Nat. Catal.* **6**, 319–331 (2023).